RSC Advances

PAPER

View Article Online
View Journal | View Issue

Cite this: *RSC Adv.*, 2024, **14**, 24874

Fabrication of a highly efficient $CuO/ZnCo_2O_4$/CNTs ternary composite for photocatalytic degradation of hazardous pollutants

Norah Alomayrah,[a] Mustabshira Ikram,[b] Sonia Zulfiqar,[cde] Sultan Alomairy,[f] Mohammed Sultan Al-Buriahi,[g] Imran Shakir,[h] Muhammad Farooq Warsi *[b] and Eric W. Cochran *[d]

Received 15th June 2024
Accepted 25th July 2024

DOI: 10.1039/d4ra04395b

rsc.li/rsc-advances

In the current study, CuO, $ZnCo_2O_4$, $CuO/ZnCo_2O_4$, and $CuO/ZnCo_2O_4$/CNTs photocatalysts were prepared to remove crystal violet (CV) and colorless pollutants (diclofenac sodium and phenol) from wastewater. Herein, sol–gel and co-precipitation methods were used to synthesize CuO and $ZnCo_2O_4$, respectively. The sonication method was used to synthesize $CuO/ZnCo_2O_4$ and a CNTs-based composite ($CuO/ZnCo_2O_4$/CNTs). From the UV-Vis spectra of CuO, $ZnCo_2O_4$, $CuO/ZnCo_2O_4$, and $CuO/ZnCo_2O_4$/CNTs, the optical band gap value was calculated to be 2.11, 2.18, 1.71 and 1.63 eV respectively. The photocatalytic results revealed that $CuO/ZnCo_2O_4$/CNTs exhibited higher degradation of 87.7% against CV dye, 82% against diclofenac sodium, and 72% against phenol as compared to other prepared photocatalysts. The $OH^{\bullet}$ radical is identified as the active species in the photocatalytic process over $CuO/ZnCo_2O_4$/CNTs. The impact of several parameters, such as pH, concentration, and catalyst dosage, has also been investigated. The better activity of the CNTs-based composite was due to the synergic effect of both $CuO/ZnCo_2O_4$ nanocomposite and carbon nanotubes. Therefore, the synthesized $CuO/ZnCo_2O_4$/CNTs photocatalyst has the potential to degrade organic wastewater effluents effectively.

1. Introduction

Water is one of the essential substances for the existence of life on the surface of the Earth.[1] The fast growth of industries has resulted in the shortage of clean water, which poses a severe threat to living organisms.[2,3] There are numerous causes of water pollution.[4,5] As a consequence of different industrial processes, oils, organic solvents, heavy metals, textiles, mining, dyes, and harmful pollutants are discharged into the water.[6,7] Dyes discharged in the water from industries have a large production cycle, slow decay, low discoloration, and toxic effects on human health and marine life. Therefore, dyes have received a lot of interest during their discharge in industrial effluents.[8] Various conventional techniques, including flocculation, adsorption, precipitation, sedimentation, chlorination, chemical oxidation, and photocatalytic degradation, have been employed to extract the harmful pigments from the industrial effluents.[9–12] Among all the techniques, photocatalytic degradation has attracted the most attention because of its simple operation, low energy consumption, low cost, low secondary pollution, and high efficiency.[13] Photocatalysis is a green, cutting-edge, quick, and affordable technology that uses semiconducting materials as photocatalysts under irradiation of light to eliminate all industrial potentially contaminates and other hazardous chemicals from water.[14,15] These materials are more effective, have a larger surface area, flexible band gaps, and require less energy to generate photo-excited states.[16,17] Excited electrons and produced holes serve as the main reactants in photocatalytic processes.[9] They interact with water and molecular oxygen to form secondary active species which interact with organic dyes and decompose them into simpler molecules.[18]

Metal oxide nanoparticles have several interesting characteristics, such as distinct electrical structures, as well as many phases, sizes, shapes, multiple oxidation states, and catalytic pollutant removal capabilities.[19,20] Copper oxide (CuO) is one of the significant p-type semiconductors among the transition-metal oxides and has gained a lot of attention because of its

[a]*Department of Physics, College of Science, Princess Nourah bint Abdulrahman University, P. O. Box 84428, Riyadh 11671, Saudi Arabia*
[b]*Institute of Chemistry, Baghdad-ul-Jadeed Campus, The Islamia University of Bahawalpur, Bahawalpur-63100, Pakistan. E-mail: farooq.warsi@iub.edu.pk*
[c]*Department of Physical Sciences, Lander University, 320 Stanley Ave, Greenwood, South Carolina 29649, USA*
[d]*Department of Chemical and Biological Engineering, Iowa State University, Sweeney Hall, 618 Bissell Road, Ames, Iowa 50011, USA. E-mail: ecochran@iastate.edu*
[e]*Department of Chemistry, Faculty of Science, University of Ostrava, 30. Dubna 22, Ostrava, 701 03, Czech Republic*
[f]*Department of Physics, College of Science, Taif University, Taif 21944, Saudi Arabia*
[g]*Department of Physics, Sakarya University, Sakarya, Turkey*
[h]*Department of Physics, Faculty of Science, Islamic University of Madinah, Madinah, 42351, Saudi Arabia*

narrow band gap.[21] CuO is a transition metal oxide with a wide range of uses in different industries, including batteries, photoelectrochemical water splitting, photodetectors, supercapacitors, chemical and biosensors, and photovoltaic devices.[22] CuO is closely related to high-Tc superconductors and has also been widely used as a potent heterogeneous catalyst to fully convert hydrocarbons into CO_2 and H_2O. CuO nanostructures have been employed in a wide range of settings, such as magnetic storage media, chemical and gas sensors, catalysis, in antitumor therapy, as biomedicine to prevent bacterial infection, and in photocatalysis to break down organic pollutants from wastewater.[23] Harish *et al.* synthesized a ZnO/CuO nanocomposite and found that the composite showed excellent efficiency for the removal of organic effluents.[24] Katal *et al.* prepared CuO films for photocatalytic degradation of MB dye.[25] Hossain *et al.* synthesized CuO/CdS by an ultrasound-assisted-wet-impregnation method and found that the nanocomposite exhibited excellent degradation capacity by degrading 75% of MB dye.[26] Atta ur Rehman *et al.* synthesized binary metal doped CuO nanocatalysts. The results revealed that the doping in CuO facilitates the excitation process and significantly increases the photocatalytic activity of the material.[27]

Mixed metal oxides that have been extensively researched have a spinel structure and have the general formula of AB_2O_4.[28] Examples of these oxides are $CuGa_2O_4$,[29] $CuFe_2O_4$,[30] $ZnFe_2O_4$,[31] $CoFe_2O_4$,[32] $MnCo_2O_4$,[33] $CoMn_2O_4$,[34] and $ZnCo_2O_4$.[35] Among these, $ZnCo_2O_4$ is a typical spinel material and has attracted a lot of attention owing to its exceptional electronic structural properties and potential use as an anode material and gas sensor.[36,37] The spinel $ZnCo_2O_4$ is a p-type semiconductor and has garnered significant interest due to its low cost, nontoxicity, earth-abundant nature, narrow energy band (E_g), and better electron conductivity as compared to single metal oxides like ZnO, Co_3O_4.[38] Because of its unique energy band structure (2.0 eV), the electrons within these bands show transition more readily. This lowers the rate of photogenerated electron–hole recombination.[39] Recent research on ZnO and other metal oxide-based nanocomposites has shown that a greater photocatalytic activity can be achieved because of the efficient transfer of charge carriers.[40] Taufique *et al.* synthesized a CuO–ZnO nanocomposite using hydrothermal approach. The results showed that the maximum photocatalytic activity achieved in the case of CuO–ZnO nanostructure.[41] Goswami *et al.* synthesized heterostructured cation-doped ZnO–$ZnCo_2O_4$ nanocomposites. The results demonstrate heterojunction interfaces, which aid in the separation and transfer of electron–hole pairs, causing increased photocatalytic activity.[42] Combinations of semiconductors, such as ZnO/$ZnCo_2O_4$,[42] $CaFe_2O_4$/$ZnCo_2O_4$,[43] and SnO_2/$ZnCo_2O_4$,[28] have also been investigated in order to improve photo-efficiency of the prepared materials. The synergistic effect of copper, zinc and cobalt, metals as CuO/$ZnCo_2O_4$ increased the catalytic activity of nanocomposite as compared to pristine CuO and $ZnCo_2O_4$. It is a facile approach to form the CuO/$ZnCo_2O_4$ nanocomposite because the electrical band structures of the two materials match perfectly.[44] The interaction of these semiconductors generally results in the formation of an inherent potential that enhances the photocatalytic effectiveness of the prepared composite. Moreover, the CuO/$ZnCo_2O_4$ nanocomposite exhibits effective separation of photogenerated electron–holes pairs because of the synergistic effects of the metals present in the composite. Zhu *et al.* synthesized a CuO/ZnO composite and found that the composite showed better photocatalytic activity as compared to pristine CuO and ZnO.[45] Jahanshahi *et al.* found that a $ZnCo_2O_4$/g-C_3N_4/Cu nanocomposite showed enhanced photocatalytic performance towards the MNZ degradation.[46]

One way to overcome the limitations and to further improve the photocatalytic properties of CuO/$ZnCo_2O_4$ is to combine it with carbonaceous nanomaterials like carbon nanotubes (CNTs),[47] reduced-graphene oxide (rGO),[48] graphene,[49] and fullerenes.[50] Carbon nanotubes (CNTs) have attracted a lot of interest in photocatalytic research because of their excellent conductivity and large surface area.[51] CNTs have been used in the synthesis of composites because of their special properties, including large specific surfaces, high tensile strength, corrosion resistance, and chemical stability. In the photocatalytic process, CNTs can separate charge carriers by capturing photoinduced electrons, thus extending their lifespan and accelerating the photocatalytic efficiency of prepared material, and leading to the effective breakdown of organic pollutants.[52] Saravanakkumar *et al.* reported the synthesis of CuO/ZnO/CNTs thin films and exhibited excellent degradation of Rhodamine-B.[53]

To the best of our knowledge, no reports exist on the synthesis of a CuO/$ZnCo_2O_4$ and CuO/$ZnCo_2O_4$/CNTs composite using the sonication route and their application in photocatalytic degradation of pollutants presented in this study. Nonetheless, in the literature, there are several studies, including the synthesis of diamond-like $ZnCo_2O_4$,[54] CuO,[19] Cu-ln-Zn-S@$ZnCo_2O_4$@ln_2O_3,[55] Cu-doped ZnO@CNTs,[56] and ZnO/$ZnCo_2O_4$.[42] Herein, we provide an efficient method for synthesizing CuO/$ZnCo_2O_4$/CNTs composite to improve the photocatalytic activity by lowering the electron–hole pair recombination rate. Various physicochemical methods have been used to characterize all the synthesized materials. This research provides a pathway to comprehend the strategic effect of composite in visible light photocatalysis.

2. Experimental

2.1. Chemicals

Copper nitrate hemi(pentahydrate) ($Cu(NO_3)_2 \cdot 2.5H_2O$, 99.5%), sodium hydroxide (NaOH), cobalt chloride hexahydrate ($CoCl_2 \cdot 6H_2O$, 98.0%), zinc nitrate hexahydrate ($Zn(NO_3)_2 \cdot 6H_2O$, 98%), oxalic acid ($C_2H_2O_4$, 99.9%), ethanol (C_2H_5OH, 96%), and carbon nanotubes (CNTs) were used for the synthesis of various photocatalysts. All chemicals were obtained from Sigma-Aldrich.

2.2. Synthesis of CuO

The sol–gel method was used for the synthesis of CuO nanoleaves. Firstly, 100 mL of 0.1 M solution of copper nitrate was prepared. The prepared solution was stirred to form a blue-colored homogenous solution. 0.2 M NaOH solution was then

added drop-wise. The solution was ultrasonicated at 80 °C for 2–3 h and then cooled at room temperature for several hours. This resulted in the formation of black-colored precipitates. Washing with ethanol was done to remove the impurities. The obtained product was calcined at 400 °C for 4 h.[57]

2.3. Synthesis of $ZnCo_2O_4$

$ZnCo_2O_4$ nanoparticles were synthesized by a typical co-precipitation method. The cobalt chloride and zinc nitrate salts were used as starting materials, ethanol (C_2H_5OH) as solvent, and oxalic acid ($C_2H_2O_4$) as complex agent. In 30 mL C_2H_5OH solution, 9 mmol $C_2H_2O_4$, 6 mmol $CoCl_2 \cdot 6H_2O$, and 3 mmol Zn $(NO_3)_2 \cdot 6H_2O$ were dissolved separately. The solutions were labeled A, B, and C respectively. Solution B and C were then added to solution A and stirred uniformly for an hour. This resulted in a turbid suspension. The pale pink precipitates were collected through centrifugation. This resultant slurry was then subjected to washing with ethanol. Drying was carried out at 120 °C for 8 h. The dried product was cooled at ambient temperature. Calcination was done at 500 °C for 2 h.[58]

2.4. Synthesis of $CuO/ZnCo_2O_4$

$CuO/ZnCo_2O_4$ nanocomposite was synthesized using an ultrasonication technique. 30 mL of distilled water containing 0.5 g CuO and 0.5 g of $ZnCo_2O_4$ were subjected to sonication for two hours. Next, the product was dried in an oven for 5 h.

2.5. Synthesis of $CuO/ZnCo_2O_4/CNTs$ composite

Fig. 1 shows the synthesis of $CuO/ZnCo_2O_4/CNTs$ using a sonication technique, 0.4 g of CuO and 0.4 g of $ZnCo_2O_4$ were dissolved in 20 mL of CNTs suspension. The mixture was subjected to sonication for 1 h and then dried at 80 °C for 5 h. The dried product was ground and used for the photocatalytic experiments.

2.6. Characterization

The crystal structure and purity of the prepared samples were examined using a Bruker D8 Advance powder diffractometer. Morphological analysis and energy dispersive X-ray (EDX) were recorded using Hitachi SU4800 field emission scanning electron microscope (FESEM). XPS measurements were performed on a Kratos Analytical-Amicus. Photocatalytic measurements were performed using a dual-beam spectrophotometer (Cary-60).

2.7. Photocatalytic activity

The degradation of diclofenac sodium (drug), phenol and CV dye (pollutant) was carried out to assess the photocatalytic performance of the fabricated samples. The photocatalytic experiment was carried out using a 200 watt tungsten bulb. 7 ppm CV solution was prepared in a 1000 mL beaker. The pH of the prepared solution was kept at 6. Four beakers containing 70 mL of CV solution and 30 mg of CuO, $ZnCo_2O_4$, $CuO/ZnCo_2O_4$, and $CuO/ZnCo_2O_4/CNTs$ were prepared respectively. The adsorption and desorption of photocatalysts and dye were

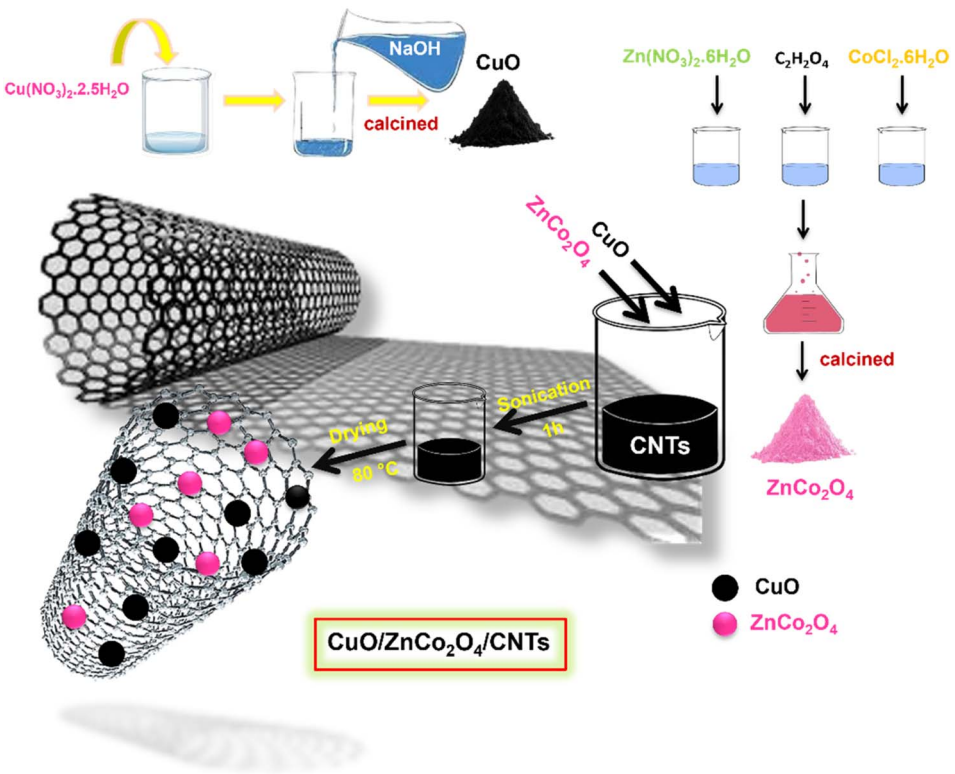

Fig. 1 Synthetic protocol for the preparation of $CuO/ZnCo_2O_4/CNTs$ composite.

carried out by placing these beakers in the dark for about 30 min. Following the dark reaction, 4 mL of the homogenous mixture was taken out of each beaker. An Agilent Cary-60 UV spectrophotometer was used to measure the UV light absorption of the solutions after the reaction mixture was centrifuged in order to settle down the suspended photocatalyst. The solution was put under a 200 watt tungsten bulb irradiation for the subsequent experiment. After every 10 min, 4 mL of sample solutions were taken out, centrifuged and their absorbance was recorded. The procedure continued for 90 min. The diclofenac sodium and phenol photodegradation process followed the same procedure. The following eqn (1) was utilized to calculate the percentage degradation, in which A_o represents the absorbance at zero minutes. A_t shows absorbance at various periods of time;

$$\text{Degradation } (\%) = 1 - \frac{A_t}{A_o} \times 100 \quad (1)$$

3. Results and discussion

3.1. X-ray diffraction (XRD) analysis

XRD analysis was used to assess the crystallinity and crystal phases of the synthesized materials.[59] Fig. 2 shows the diffraction pattern of CuO, $ZnCo_2O_4$, $CuO/ZnCo_2O_4$, and $CuO/ZnCo_2O_4$/CNTs. Fig. 2(a) shows the XRD pattern of CuO. All of the diffraction peaks are assigned to the CuO monoclinic phase (lattice constants a = 4.74722 Å, b = 3.320797 Å, and c = 5.094737 Å), which matches well with JCPDS Card No. 048-1548.[60] The diffraction peaks at 2θ values of 32.5°, 35.4°, 38.7°, 48.7°, 53.4°, 58.2°, 61.5°, 66.2°, 68.1°, 72.3°, and 75.2° correspond to (110), (002), (111), (20$\bar{2}$), (020), (202), and (11$\bar{3}$), (31$\bar{1}$), (220), (311), and (22$\bar{2}$) *hkl* planes. In Fig. 2(b), XRD data shows the diffraction planes of $ZnCo_2O_4$. The cubic phase of $ZnCo_2O_4$ is responsible for all the diffraction peaks. The diffraction peaks at 2θ values of 31.2°, 36.8°, 38.4°, 44.7°, 48.9°, 55.5°, 59.2°, 65.1°, and 77.2° correspond to (220), (311), (222), (400), (331), (422), (511), (440), and (553) *hkl* planes. These peaks are matched well with JCPDS 023-1390.[61] There are some extra peaks and these remaining peaks exhibited the presence of

Table 1 Structural parameters of CuO and $ZnCo_2O_4$

Sample	CuO	$ZnCo_2O_4$
Crystal system	Monoclinic	Cubic
Lattice constant a (Å)	4.747	8.299
Lattice constant b (Å)	3.320	—
Lattice constant c (Å)	5.094	—
Cell volume V (Å)^3	78.67	571.58
Space group	$C2/c$	$Fd3m$

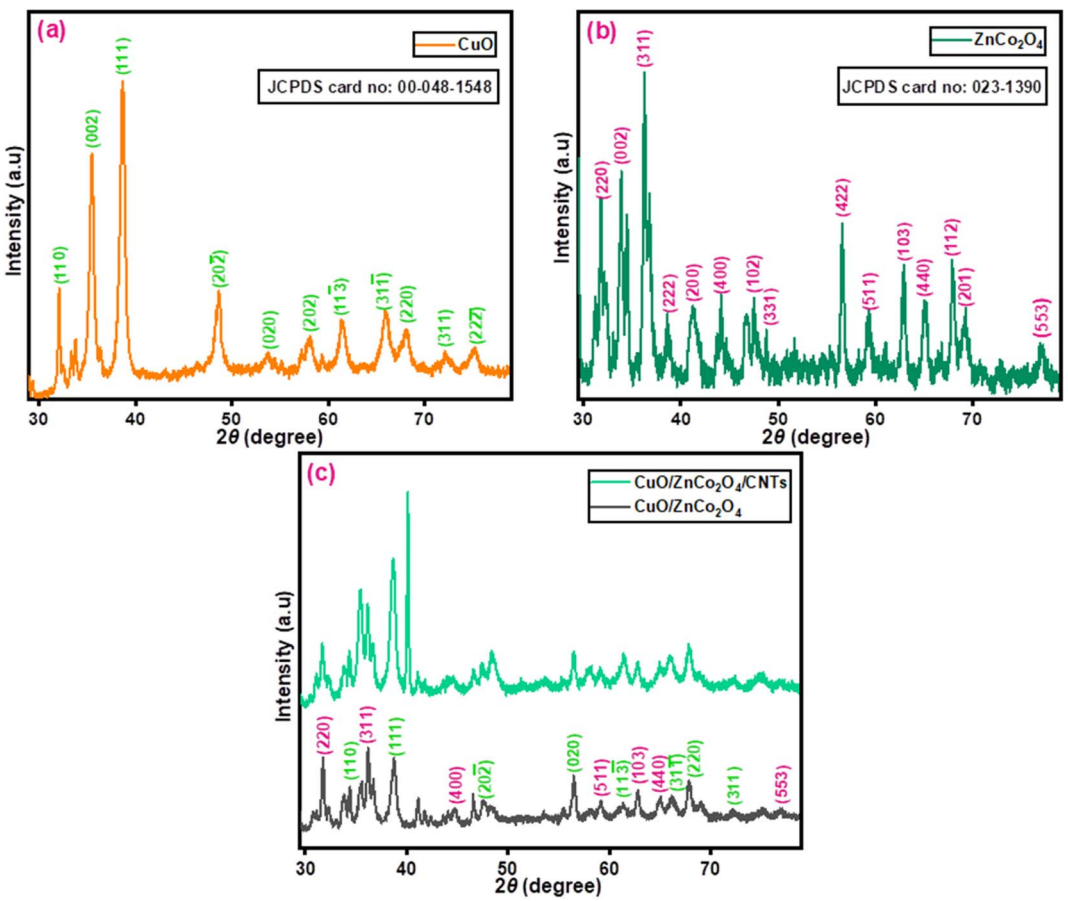

Fig. 2 XRD patterns of (a) CuO (b) $ZnCo_2O_4$ (c) $CuO/ZnCo_2O_4$ and $CuO/ZnCo_2O_4$/CNTs.

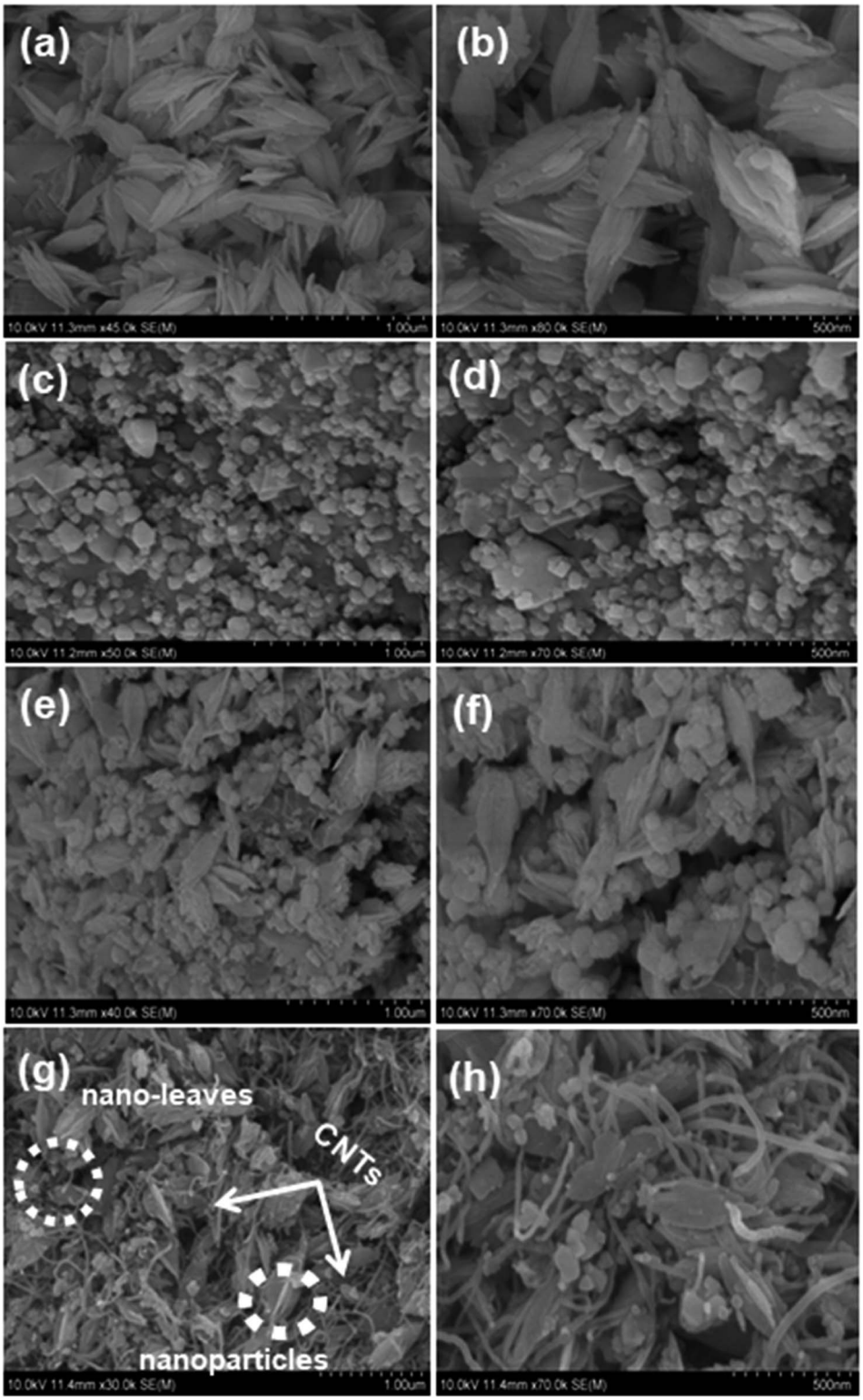

Fig. 3 FESEM images of (a and b) CuO (c and d) $ZnCo_2O_4$ (e and f) $CuO/ZnCo_2O_4$ and (g and h) $CuO/ZnCo_2O_4$/CNTs.

ZnO. These peaks are associated with the (002), (102), (103), (112), and (201) *hkl* planes (JCPDS 00-036-1451). These peaks are matched with the diffraction peaks at $2\theta = 34.4°$, 47.5°, 62.8°, 67.9°, and 69.1° respectively. A peak at 41.2° corresponding to (200) *hkl* plane is mainly because of CoO (JCPDS 48-1719).[62] As in Fig. 2(c), the XRD spectrum of $CuO/ZnCo_2O_4$ includes combined peaks of both CuO and $ZnCo_2O_4$. The introduction of CNTs in $CuO/ZnCo_2O_4$ has no significant effect on the structure

of $CuO/ZnCo_2O_4$ as seen in Fig. 2(c). Peak shifting and intensity alteration was observed in the XRD pattern of $CuO/ZnCo_2O_4$/CNTs Fig. 2(c). Using the cell software, the lattice parameters of CuO and $ZnCo_2O_4$ were determined and presented in Table 1. The crystallite/grain sizes were calculated by using the following Debye–Scherrer eqn (2).[63]

$$D = \frac{k\lambda}{\beta \cos \theta} \quad (2)$$

where D represents the average particle size, λ corresponds to the X-ray wavelength, b is the full-width at half-maximum, θ represents the diffraction angle, and K is a constant (0.89), respectively. The grain sizes calculated using the aforementioned eqn (2), for CuO, $ZnCo_2O_4$, $CuO/ZnCo_2O_4$, and $CuO/ZnCo_2O_4$/CNTs were found to be 12.9 nm, 19.1 nm, 9.8 nm, and 8.1 nm, respectively. The literature indicates that a sample with a smaller grain size has a greater ability for charges to flow across it.[64] Eqn (3) was used to calculate the surface area of CuO and $ZnCo_2O_4$.[65]

$$\text{Surface area} = \frac{6000}{\text{G.S} \times \rho_x} \quad (3)$$

The extent to which grain boundaries are broken down affects surface area. The CuO and $ZnCo_2O_4$ had a surface area of 115 m^2 g^{-1}, 92.3 m^2 g^{-1}, with a grain size of 12.9 nm and 19.1 nm, respectively. Arun Kumar *et al.* synthesized nanocomposite and found that the nanocomposite had a small grain size of 0.50 nm as compared to pristine TiO_2 (4.74 nm) and SiO_2 (0.63 nm). Their

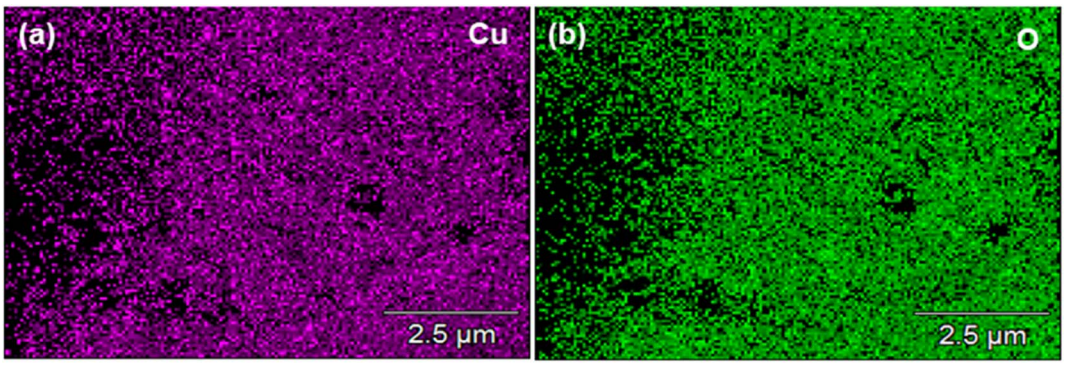

Fig. 4 Energy-dispersive X-ray elemental maps of CuO (a) Cu and (b) O.

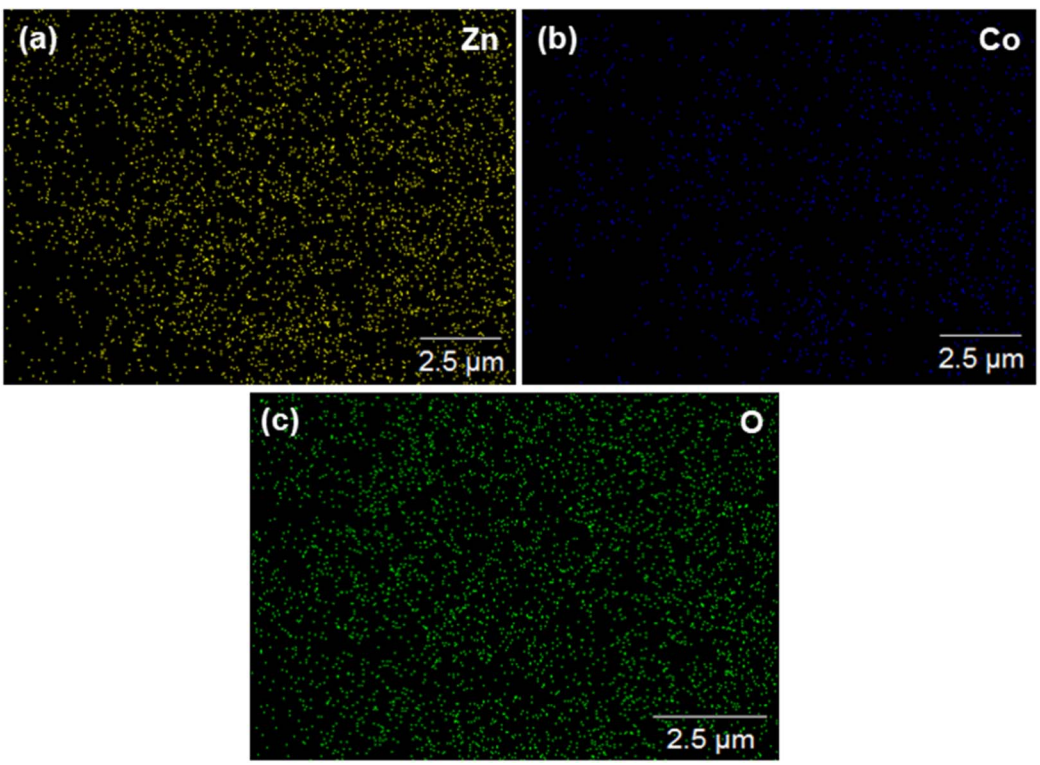

Fig. 5 Energy-dispersive X-ray elemental maps of $ZnCo_2O_4$((a) Zn (b) Co and (c) O.

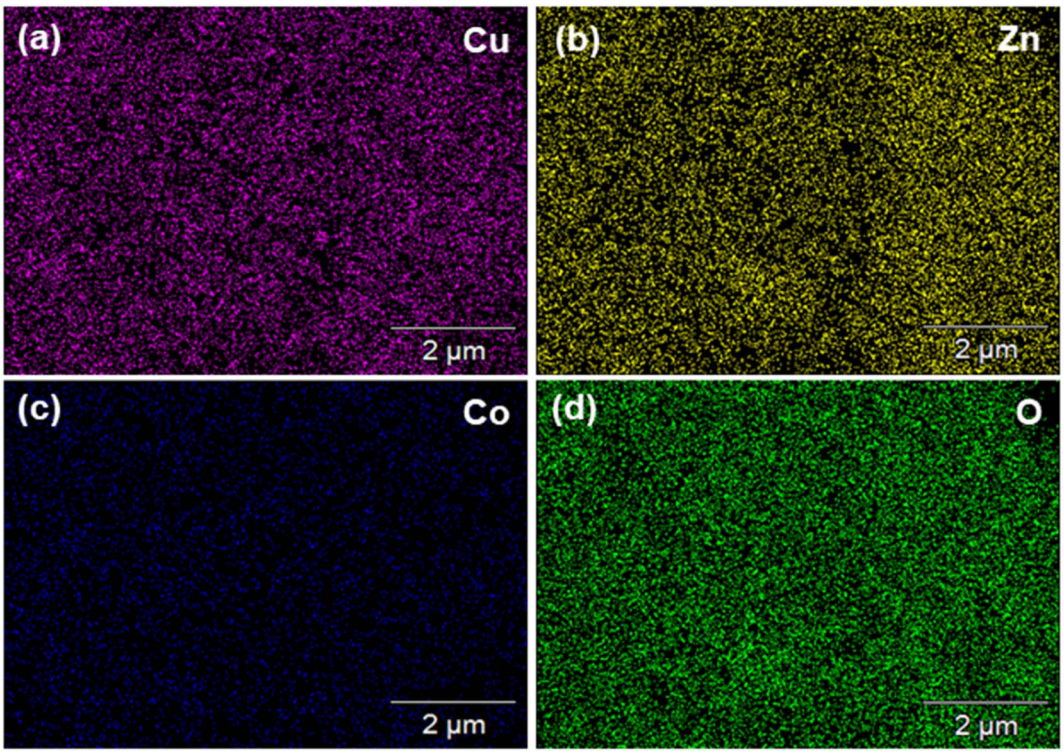

Fig. 6 Energy-dispersive X-ray elemental maps of $CuO/ZnCo_2O_4$ (a) Cu (b) Zn (c) Co and (d) O.

BET analysis showed that nanocomposite showed a large surface area of 303 $m^2 g^{-1}$ as compared to pristine samples.[66]

These results revealed that surface area is correlated with grain size. The smaller the value of grain size, the greater the surface area. $CuO/ZnCo_2O_4$ and $CuO/ZnCo_2O_4$/CNTs have small grain sizes as compared to CuO and $ZnCo_2O_4$, so they will offer higher surface area and an increased number of sites where degradation of pollutants occur. It was further validated through Thakur *et al.* research on PANI/CNTs/MoS_2. It was found that the surface area of PANI was increased from 17.85 $m^2 g^{-1}$ to 23.14 $m^2 g^{-1}$ resulting from the incorporation of CNTs into the PANI matrix.[67] Guo *et al.* synthesized TiO_2–CNTs composite and found that CNTs-based composite has small crystallite size as compared to pristine TiO_2.[68]

3.2. FESEM and EDX analysis

Field emission scanning electron microscopy (FESEM) was used to investigate the apparent morphology of the synthesized samples.[69] Fig. 3 shows the FESEM micrographs of CuO, $ZnCo_2O_4$, $CuO/ZnCo_2O_4$, and $CuO/ZnCo_2O_4$/CNTs that were taken at different magnifications. Fig. 3(a and b) shows the nano-leaves like morphology of CuO. Nanoparticles are clearly seen in the micrographs of $ZnCo_2O_4$ Fig. 3(c and d). The presence of both nano-leaves and nanoparticles in Fig. 3(e and f) suggests the successful synthesis of $CuO/ZnCo_2O_4$. Fig. 3(g and h) validates the successful integration of CNTs into the $CuO/ZnCo_2O_4$ matrix, leading to the synthesis of the $CuO/ZnCo_2O_4$/CNTs composite. The presence of nanotubes, nano-leaves, and nanoparticles can be clearly seen in Fig. 3(g and h). The addition of carbon nanotubes into the $CuO/ZnCo_2O_4$ matrix further increases the surface area and number of active sites, thus improving the degradation of harmful pollutants.

EDX analysis further verified the purity and chemical structure of the prepared samples. The EDX elemental maps of CuO, $ZnCo_2O_4$, $CuO/ZnCo_2O_4$, and $CuO/ZnCo_2O_4$/CNTs are shown in Fig. 4–7, respectively. EDX elemental maps of CuO verified the presence of Cu and O elements. Whereas the EDX maps of $ZnCo_2O_4$ reveal the presence of Zn, Co, and O elements. The EDX results of $CuO/ZnCo_2O_4$ and $CuO/ZnCo_2O_4$/CNTs also confirm the formation of the synthesized materials. The elemental analysis of the prepared samples shows the prominent signals for Cu, Zn, Co, O, and additionally C in the case of CNTs composite. Table 2 shows the elemental data of all the prepared samples.

3.3. X-ray photoelectron spectroscopic (XPS) analysis

The chemical and surface constituents of the fabricated samples were identified by means of XPS analysis.[70] Fig. 8 (a–e) shows the XPS spectrum along with the binding energies and the presence of elements distributed on the surface of the sample. In the C 1s spectrum, three prominent peaks of sp^2 hybridized carbon (C_I), sp^3 hybridized carbon (C_{II}), and –COO bond (C_{III}) appeared with the binding energies of 284.6 eV, 285.5 eV, and 288.7 eV. The XPS spectrum of the sample clearly indicates the presence of CNTs as shown in Fig. 8(a). Additionally, the O 1s XPS spectrum shows two peaks at 531.9 eV and 533.1 eV, which are assigned to the crystal lattice oxygen (O_I) and adsorbed oxygen (O_{II}), respectively, as can be seen in

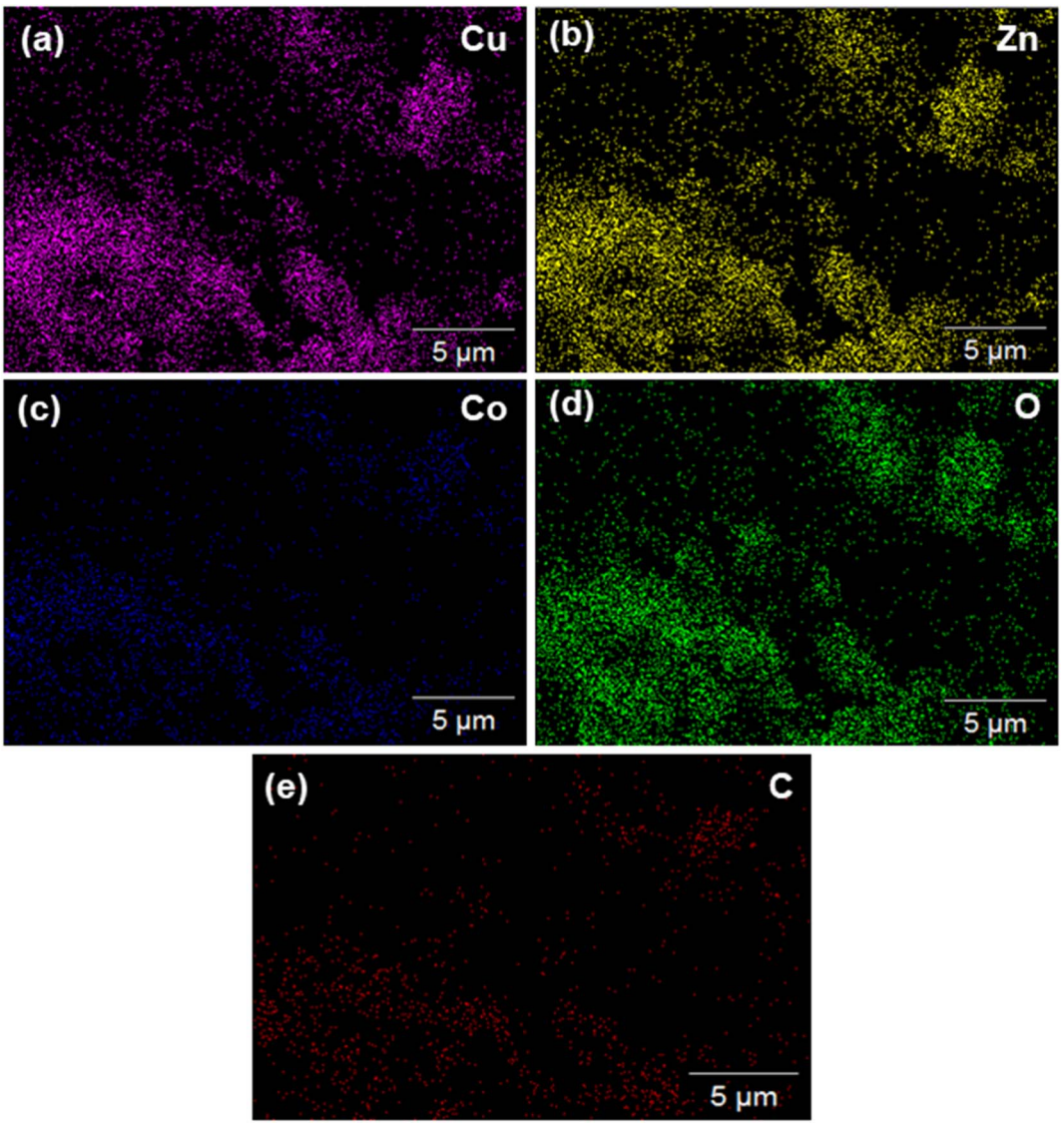

Fig. 7 Energy-dispersive X-ray elemental maps of CuO/$ZnCo_2O_4$/CNTs (a) Cu (b) Zn (c) Co (d) O and (e) C.

Table 2 Elemental data of CuO, $ZnCo_2O_4$, CuO/$ZnCo_2O_4$, and CuO/$ZnCo_2O_4$/CNTs photocatalysts

Sr. no.	Sample name	Elements	Atom%	wt%
1	CuO	Cu	40.86	73.30
		O	59.14	26.70
2	$ZnCo_2O_4$	Zn	29.02	52.97
		Co	12.78	21.03
		O	58.20	26.00
3	CuO/$ZnCo_2O_4$	Cu	8.43	16.61
		Zn	21.15	42.85
		Co	4.22	7.71
		O	66.20	32.83
4	CuO/$ZnCo_2O_4$@CNTs	Cu	14.29	29.98
		Zn	14.67	31.66
		Co	2.79	5.43
		O	44.55	23.53
		C	23.70	9.40

Fig. 8(b).[71] In the Co 2p spectrum, two distinctive peaks at 781 eV and 796.4 eV correspond to the Co $2p_{3/2}$ and Co $2p_{1/2}$ with two satellite peaks having the binding energies of 782.6 eV and 797 eV, respectively, as shown in Fig. 8(c).[72] Moreover, two peaks of Cu $2p_{3/2}$ and Cu $2p_{1/2}$ with the binding energies of 934.4 eV and 954.2 eV were seen in the XPS spectrum of Cu 2p as seen in Fig. 8(d). In addition, two satellite peaks appeared at 943.2 eV and 962.6 eV in Cu 2p spectra. In Fig. 8(e) Zn 2p indicates two peaks of $2p_{3/2}$ and $2p_{1/2}$ having the binding energy of 1022.2 eV and 1045.4 eV respectively.

3.4. Optical analysis

The optical spectra of CuO, $ZnCo_2O_4$, CuO/$ZnCo_2O_4$, and CuO/$ZnCo_2O_4$/CNTs are shown in Fig. 9(a–d), respectively. Within the 200–300 nm range, the produced samples displayed the highest absorption. The following eqn (4) was used to determine the band gap;

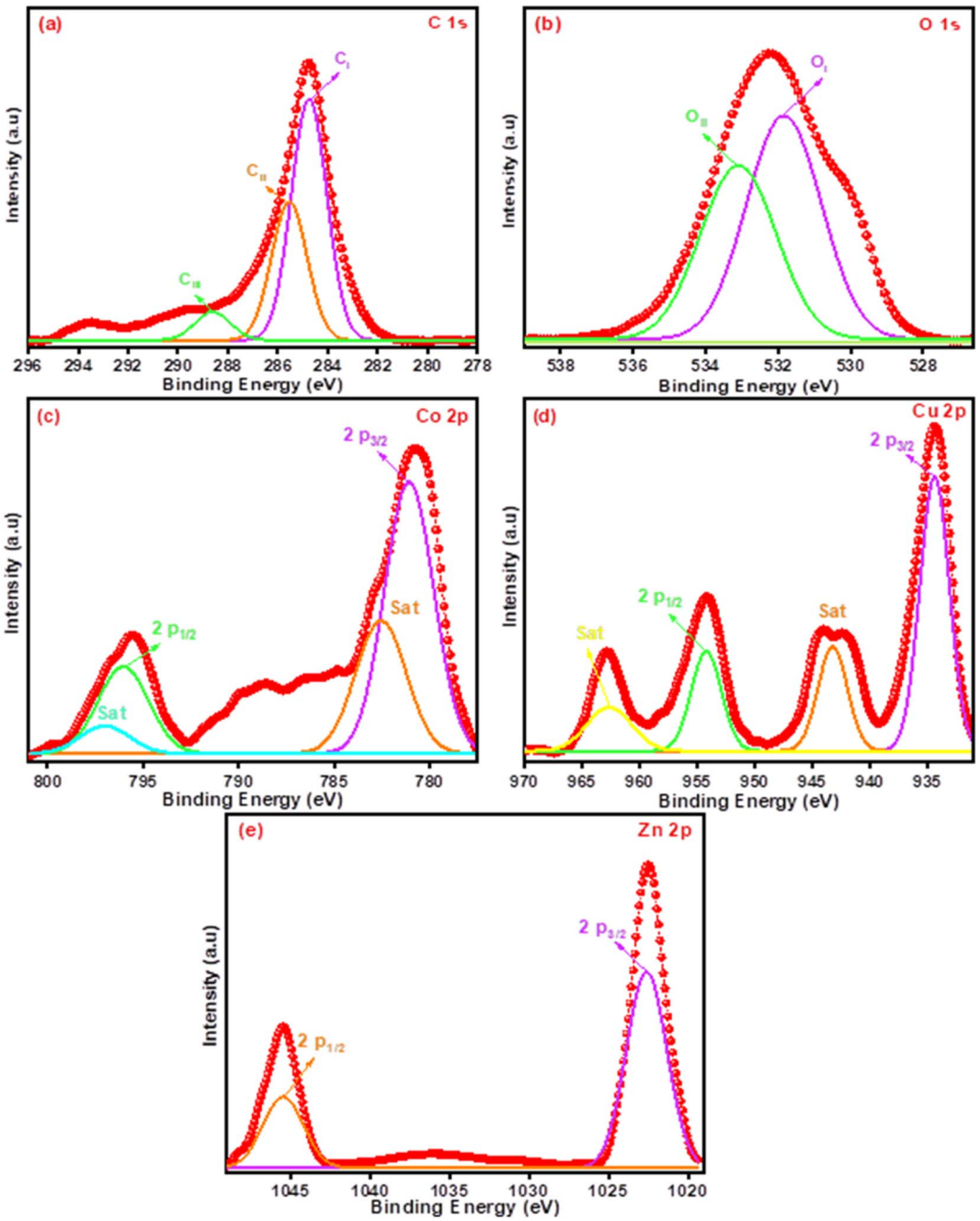

Fig. 8 High-resolution XPS spectra of (a) C 1s, (b) O 1s, (c) Co 2p, (d) Cu 2p, and (e) Zn 2p in CuO/$ZnCo_2O_4$@CNTs.

$$(\alpha h\nu)^{1/n} = A(h\nu - E_g) \quad (4)$$

where α represents the absorption coefficient, ν is the energy of the photon, and A demonstrates constant of proportionality. The band gap energy of the synthesized photocatalysts was analyzed to determine the effectiveness of the catalysts in dye degradation.[73] In the literature, the band gap energy ranging from 1.23 to 3.26 eV is required for photocatalysts to function effectively.[74] A graph is plotted between $h\nu$ and $(\alpha h\nu)^2$. The optical band gap energies obtained from the Tauc plots by extrapolating the curves in the direction of the x-axis are displayed in Fig. 10. It was observed that CuO, $ZnCo_2O_4$, CuO/$ZnCo_2O_4$ and CuO/$ZnCo_2O_4$/CNTs have band gap energies of 2.11, 2.18, 1.71 and 1.63 eV respectively.

3.5. Electrochemical impedance spectroscopic (EIS) analysis

Electrochemical impedance spectroscopy (EIS) was used to study the R_{ct} and R_s values of the prepared samples. Using the potentiostat half-cell structure and an alkaline electrolyte (1 M KOH), the value of R_s was determined. Nyquist plot (Fig. 11) generally displays the resistance of the interface layer at the electrode surface, where Z' denotes actual resistance and Z''

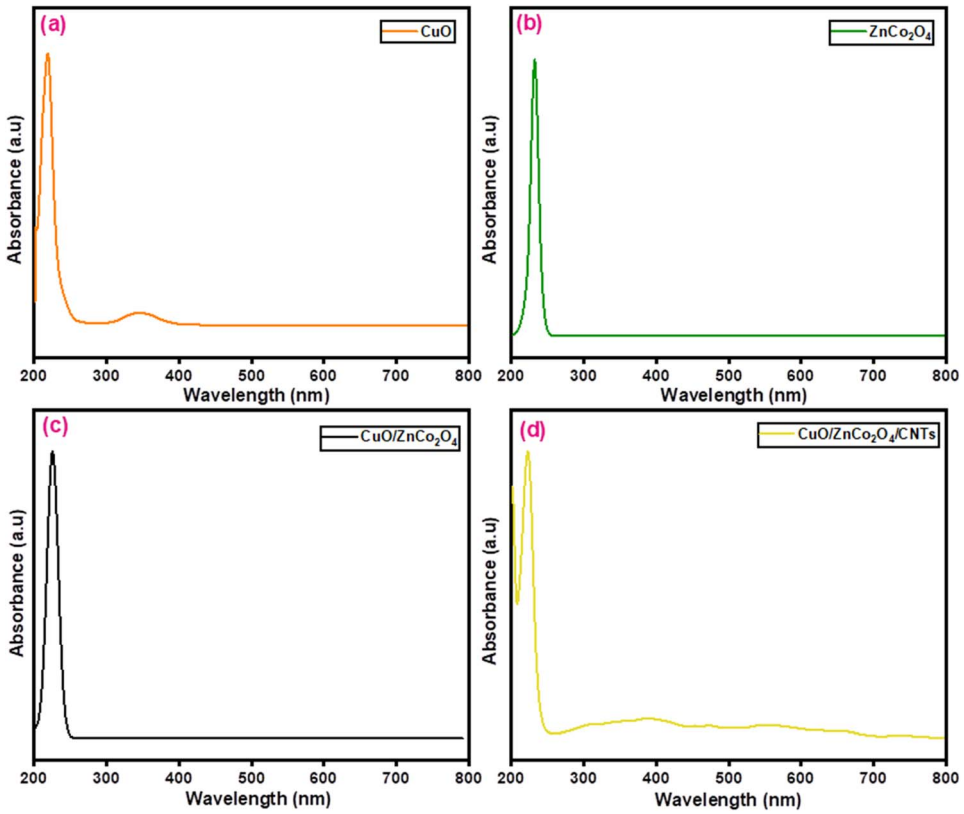

Fig. 9 The UV-Visible spectral profiles of (a) CuO (b) $ZnCo_2O_4$, (c) $CuO/ZnCo_2O_4$ and (d) $CuO/ZnCo_2O_4$/CNTs.

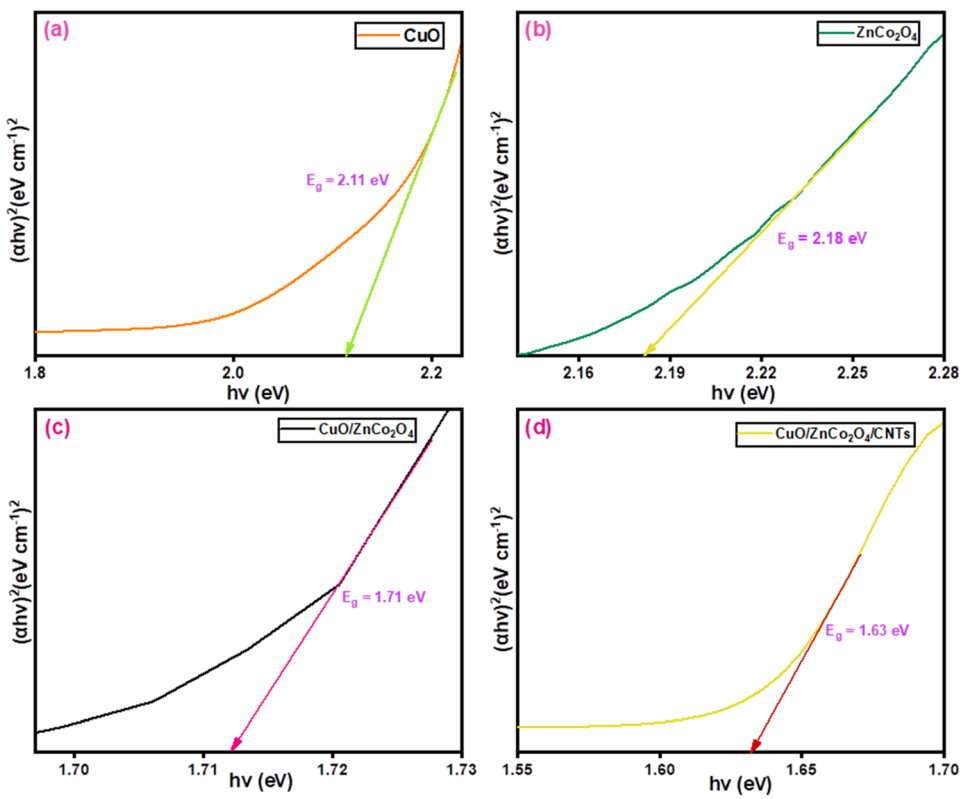

Fig. 10 Tauc plots for (a) CuO (b) $ZnCo_2O_4$, (c) $CuO/ZnCo_2O_4$ and (d) $CuO/ZnCo_2O_4$/CNTs.

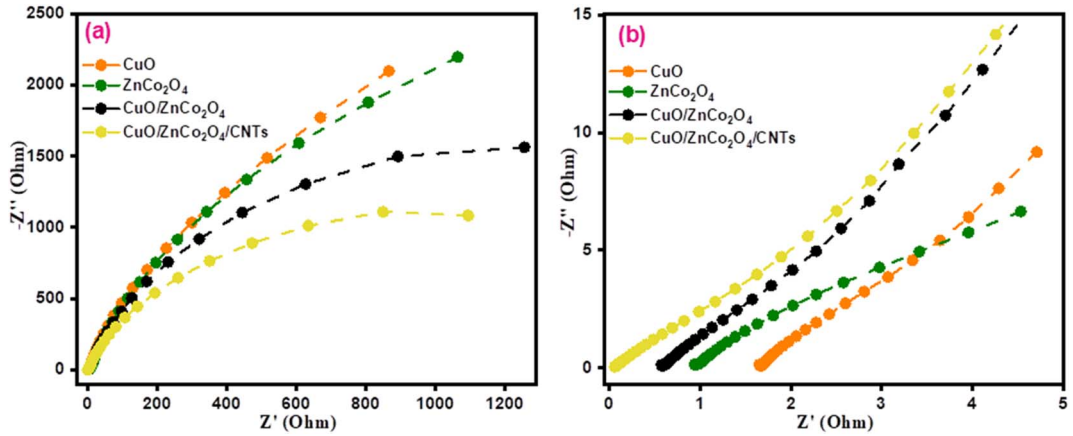

Fig. 11 EIS measurements: (a) Nyquist plots for all fabricated photocatalysts. (b) Magnified high-frequency region of Nyquist plots.

denotes imaginary resistance. For CuO, $ZnCo_2O_4$, CuO/$ZnCo_2O_4$, and CuO/$ZnCo_2O_4$/CNTs, the R_s values are 1.68 Ω, 0.94 Ω, 0.56 Ω, and 0.04 Ω respectively. In EIS spectra, the arc radius depicts the charge transfer rate. A smaller arc radius of CuO/$ZnCo_2O_4$/CNTs shows a higher charge-transfer process because photogenerated electrons and holes are effectively separated, which enhances the electron transfer during the redox reaction. Therefore, the low R_s value of CuO/$ZnCo_2O_4$/CNTs, as compared to other electrode materials, exhibits high conductance and allows the degradation of organic contaminants more effectively by photocatalysis.

3.6. Mott–Schottky analysis

In order to enhance our understanding of the electrical nature and intrinsic characteristics of semiconductor materials, Mott–Schottky technique was used. This analysis was used to examine

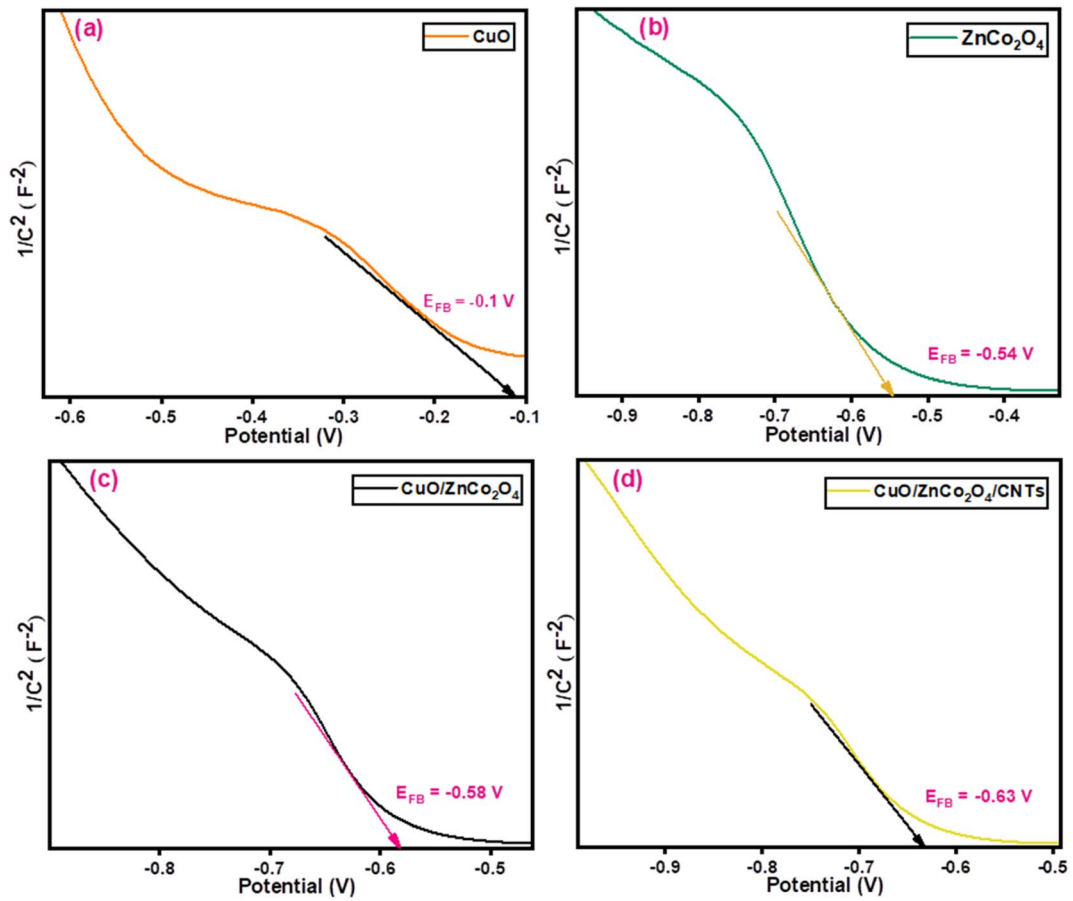

Fig. 12 Mott–Schottky diagrams of (a) CuO (b) $ZnCo_2O_4$ (c) $CuO/ZnCo_2O_4$, and (d) $CuO/ZnCo_2O_4$/CNTs.

the type of semiconductor (p-type or n-type). A GAMRY Interface 5000 E was used to conduct the measurements. The potential *vs.* $1/C^2$ provides the value of the flat band potential for CuO, $ZnCo_2O_4$, $CuO/ZnCo_2O_4$, and $CuO/ZnCo_2O_4$/CNTs electrodes (Fig. 12). The following formula (5) was used to calculate the flat band potential (E_{FB}):

$$\frac{1}{C^2} = \frac{2}{\varepsilon\varepsilon_o N_D\left(E - E_{FB} - \frac{K_b T}{q}\right)} \quad (5)$$

Fig. 12 illustrates the negative slopes for CuO, $ZnCo_2O_4$, $CuO/ZnCo_2O_4$, and $CuO/ZnCo_2O_4$/CNTs, demonstrating that they are p-type semiconducting materials. The values of flat band potential (E_{FB}) for CuO, $ZnCo_2O_4$, $CuO/ZnCo_2O_4$, and $CuO/ZnCo_2O_4$/CNTs are −0.10, −0.54, −0.58, and −0.63 V respectively. In comparison to other synthesized nanocatalysts, the $CuO/ZnCo_2O_4$/CNTs has a higher negative flat band potential value as shown in Fig. 12. This negative flat band potential value promotes rapid charge movement in the semiconducting material and greatly inhibits charge carrier recombination as compared to other electrode materials. E_{FB} affects redox processes, kinetics, and alignment of energy levels. A higher negative E_{FB} value indicates a faster redox reaction. Therefore, $CuO/ZnCo_2O_4$/CNTs show a faster redox process as compared to CuO, $ZnCo_2O_4$, and $CuO/ZnCo_2O_4$.

4. Photocatalytic studies

4.1. Photodegradation of crystal violet

The photodegradation activity of CuO, $ZnCo_2O_4$, $CuO/ZnCo_2O_4$, and $CuO/ZnCo_2O_4$/CNTs was investigated using crystal violet, a colored organic pollutant. Fig. 13 shows the absorption spectra of the fabricated samples. Fig. 14(a and b) shows the kinetics plots for the photodegradation of crystal violet by various photocatalysts. $CuO/ZnCo_2O_4$/CNTs, $CuO/ZnCo_2O_4$, $ZnCo_2O_4$, and CuO were able to degrade 87.7%, 78%, 61.5%, and 45.6% of the crystal violet dye, respectively. Among the other photocatalysts, $CuO/ZnCo_2O_4$/CNTs has the highest photocatalytic efficiency as shown in Fig. 14(c). The rate constants for crystal violet dye degradation by CuO, $ZnCo_2O_4$, $CuO/ZnCo_2O_4$, and $CuO/ZnCo_2O_4$/CNTs are shown in Fig. 14(d) as 0.006, 0.009, 0.016, and 0.022 min^{-1}, respectively. The highest value of rate constant in the case of CNTs-based composite is mainly because of the synergetic effect of both CNTs and $CuO/ZnCo_2O_4$ that increase the effectiveness of this photocatalyst compared to $CuO/ZnCo_2O_4$ that has low photodegradation efficiency. Introduction of CNTs offers enhanced surface area and active sites to maximize adsorption while lowering the rate at which photogenerated species recombine. By forming a composite of CuO with $ZnCo_2O_4$, the band gap was reduced as compared to pure CuO and $ZnCo_2O_4$. Table 3 shows various parameters for CV degradation by the prepared photocatalysts.

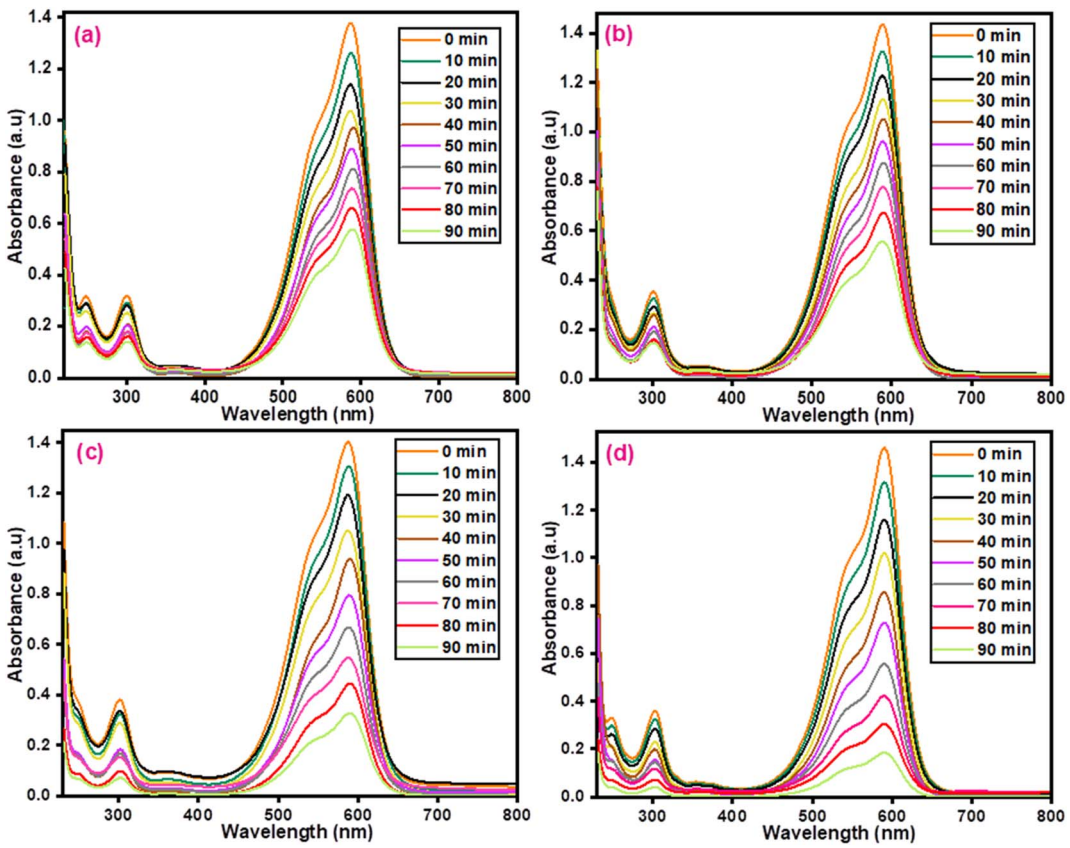

Fig. 13 Absorption spectra of (a) CuO (b) $ZnCo_2O_4$ (c) $CuO/ZnCo_2O_4$, and (d) $CuO/ZnCo_2O_4$/CNTs for CV dye degradation.

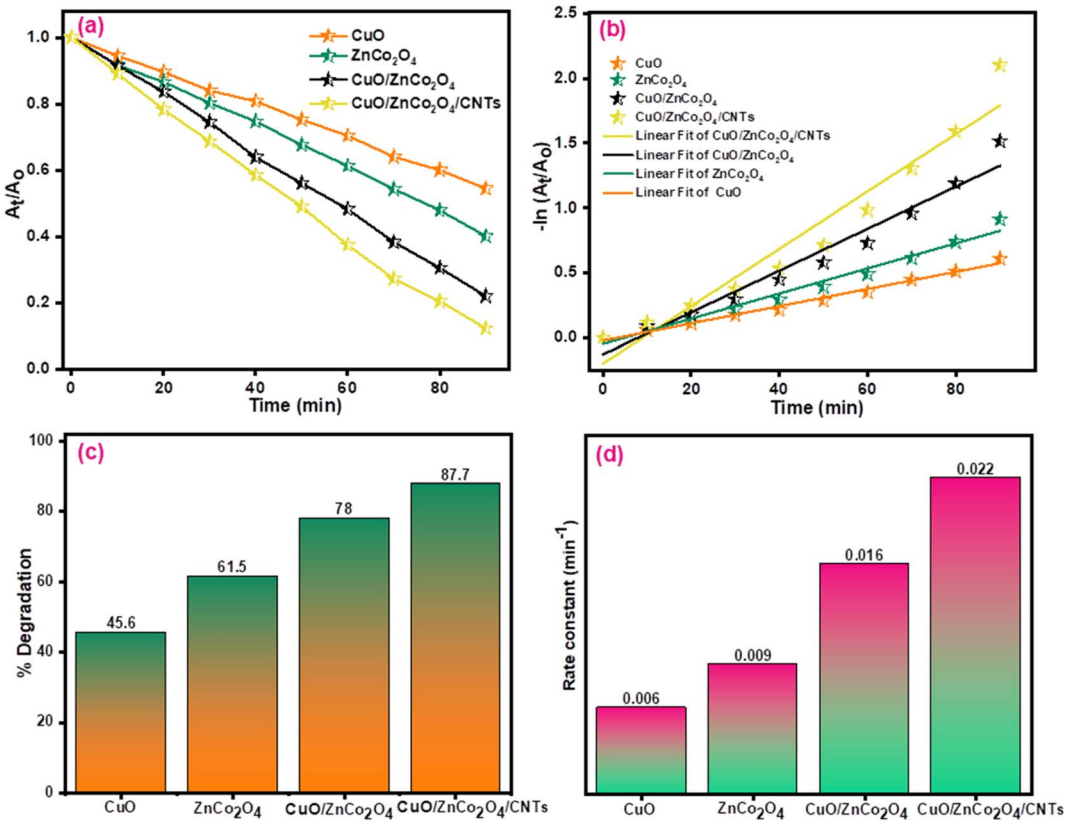

Fig. 14 (a and b) Kinetic plots (c) % degradation and (d) rate constant plot for CV dye degradation using CuO, $ZnCo_2O_4$, $CuO/ZnCo_2O_4$, and $CuO/ZnCo_2O_4$/CNTs.

Table 3 Calculated parameters for CV dye degradation using various photocatalysts

Photocatalyst	Degradation (%)	k (min^{-1})	$t_{1/2}$ (min)	R^2
CuO	45.6	0.006	115.5	0.945
$ZnCo_2O_4$	61.5	0.009	77.0	0.960
$CuO/ZnCo_2O_4$	78	0.016	43.3	0.976
$CuO/ZnCo_2O_4$/CNTs	87.7	0.022	31.5	0.989

Table 4 shows the comparison of the photocatalytic activity of already reported catalysts with the materials synthesized in this work.

The kinetics was examined using the eqn (6);

$$-\ln[A_t/A_o] = kt \quad (6)$$

Eqn (7) was used to calculate the half-life;

Table 4 Comparison of photocatalytic activity of already reported catalysts with current study

Sr. no.	Photocatalysts	Pollutant	Light source	Degradation (%)	References
1	CuO	4-Nitrophenol	Visible light	72%	75
2	$ZnCo_2O_4$	MB	Sunlight	41.97%	76
3	Ag–$ZnCo_2O_4$	MB	Sunlight	58.02%	76
4	$ZnCo_2O_4$	CV	Visible light	84.3%	77
5	$Ti_2C/ZnCo_2O_4$	CR	Visible light	78%	78
6	$CNTs/Cu_xO$	MB	LED light	84%	79
7	ZnO/CuO	CV	Hg-vapor lamp	90%	80
8	ZnO/CuO/Ag	MO	Xe/Hg 1000W	52.34%	81
9	CuO	CV	Tungsten bulb	45.6%	Current work
10	$ZnCo_2O_4$	CV	Tungsten bulb	61.5%	Current work
11	$CuO/ZnCo_2O_4$	CV	Tungsten bulb	78%	Current work
12	$CuO/ZnCo_2O_4$/CNTs	CV	Tungsten bulb	87.7%	Current work

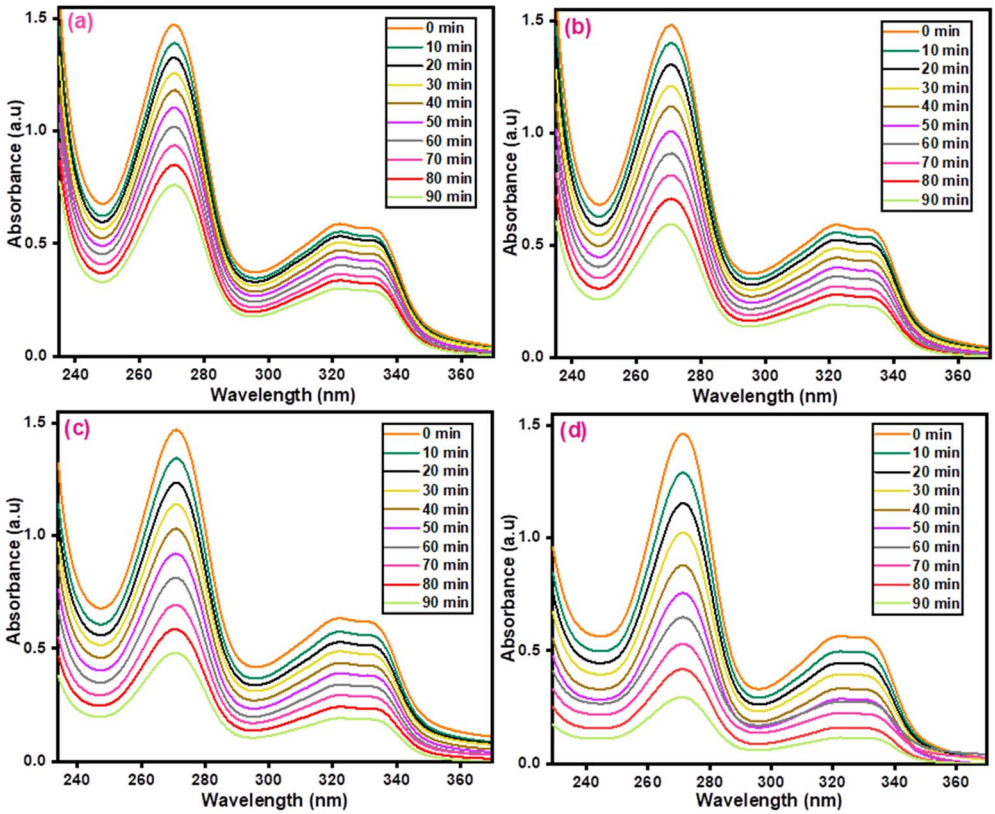

Fig. 15 Absorption spectra of (a) CuO (b) $ZnCo_2O_4$ (c) $CuO/ZnCo_2O_4$, and (d) $CuO/ZnCo_2O_4$/CNTs for diclofenac sodium degradation.

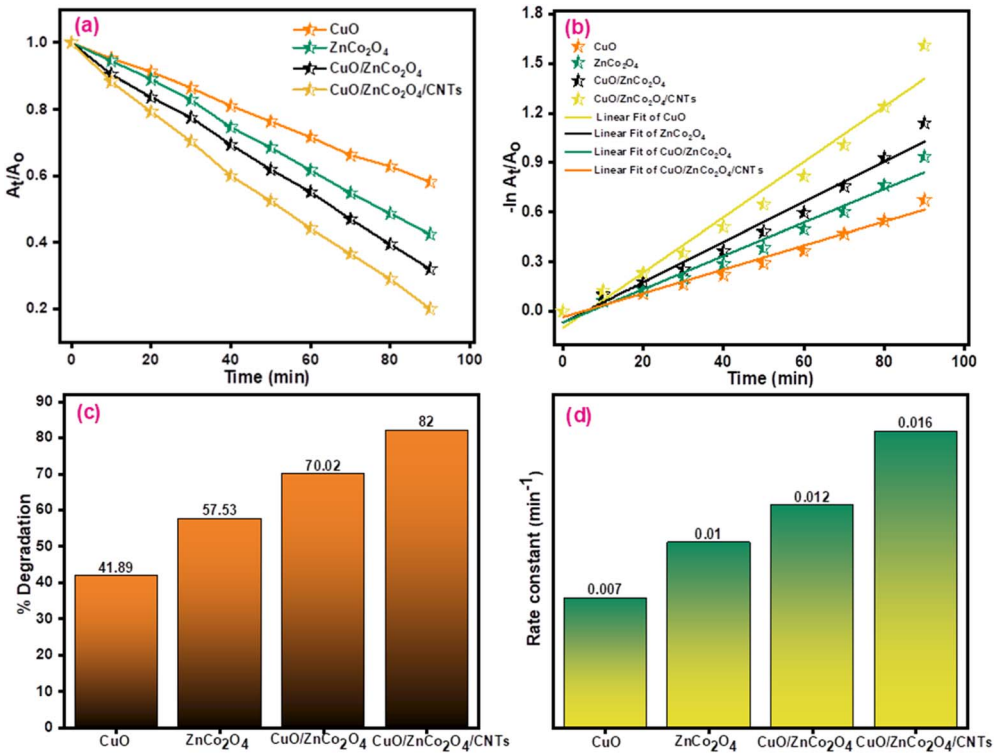

Fig. 16 (a and b) Kinetic plots (c) % degradation, and (d) rate constant plot for diclofenac sodium degradation using CuO, $ZnCo_2O_4$, $CuO/ZnCo_2O_4$, and $CuO/ZnCo_2O_4$/CNTs.

Table 5 Calculated parameters for diclofenac sodium degradation using various photocatalysts

Photocatalyst	Degradation (%)	k (min^{-1})	$t_{1/2}$ (min)	R^2
CuO	41.89	0.007	99.01	0.979
$ZnCo_2O_4$	57.53	0.010	69.3	0.971
$CuO/ZnCo_2O_4$	70.02	0.012	57.75	0.973
$CuO/ZnCo_2O_4$/CNTs	82	0.016	43.31	0.966

$$t_{1/2} = \frac{\ln 2}{k} = \frac{0.6931}{k} \quad (7)$$

4.2. Photodegradation of diclofenac sodium

The photocatalytic performance of the prepared photocatalysts was investigated for the degradation of diclofenac sodium. Absorption plots are shown in Fig. 15(a–d). Fig. 16(a and b) shows the kinetics profiles for the diclofenac sodium degradation. The rate constant values in the case of CuO, $ZnCo_2O_4$, $CuO/ZnCo_2O_4$, and $CuO/ZnCo_2O_4$/CNTs photocatalysts were found to be 0.007, 0.01, 0.012, and 0.016 min^{-1}. The % degradation values using the prepared photocatalysts are shown in Fig. 16(c). The maximum degradation of diclofenac sodium was found to be 82% using $CuO/ZnCo_2O_4$/CNTs photocatalyst, respectively. Composite with CNTs shows higher degradation as compared to other prepared catalysts. The degradation parameters for diclofenac sodium are displayed in Table 5.

4.3. Photodegradation of phenol

The photocatalytic activity of the as-prepared CuO, $ZnCo_2O_4$, $CuO/ZnCo_2O_4$, and $CuO/ZnCo_2O_4$/CNTs photocatalysts was investigated through the degradation of colorless pollutant such as phenol. The absorption plots of prepared photocatalysts are shown in Fig. 17. The rate constant for each prepared photocatalyst was determined using the linear plots, and the results are shown in Fig. 18(d) and Table 6. The rate constants for the photodegradation of phenol in the presence of CuO, $ZnCo_2O_4$, $CuO/ZnCo_2O_4$, and $CuO/ZnCo_2O_4$/CNTs photocatalysts were found to be 0.007, 0.009, 0.010, and 0.014, respectively. Fig. 18(a and b) shows the kinetics plots for the degradation of phenol. The removal percentage of phenol in the presence of CuO, $ZnCo_2O_4$, $CuO/ZnCo_2O_4$, and $CuO/ZnCo_2O_4$/CNTs photocatalysts was calculated as 51%, 57.8%, 64.3%, and 72%, respectively (Fig. 18(c)).

4.4. Recyclability experiment

A recyclability experiment was conducted to assess the stability of the fabricated photocatalyst ($CuO/ZnCo_2O_4$/CNTs) towards

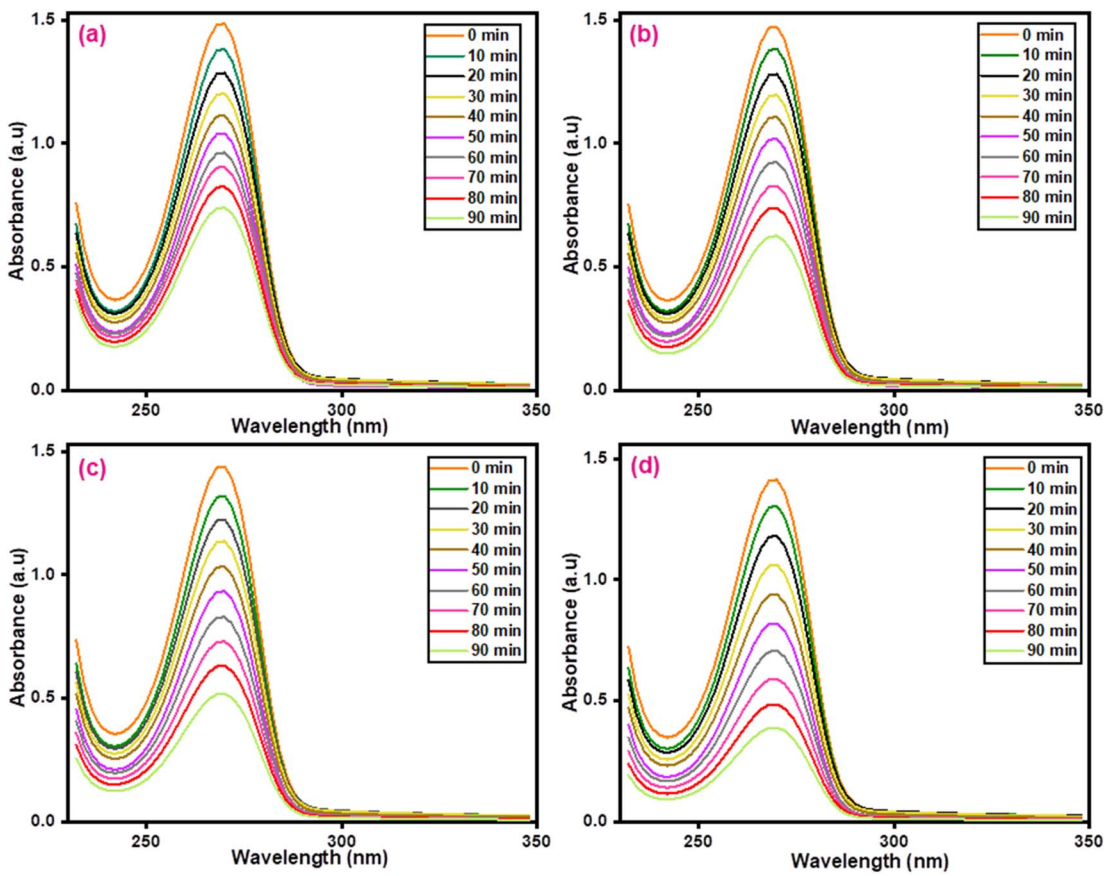

Fig. 17 Absorption spectra of (a) CuO (b) $ZnCo_2O_4$ (c) $CuO/ZnCo_2O_4$, and (d) $CuO/ZnCo_2O_4$/CNTs for phenol degradation.

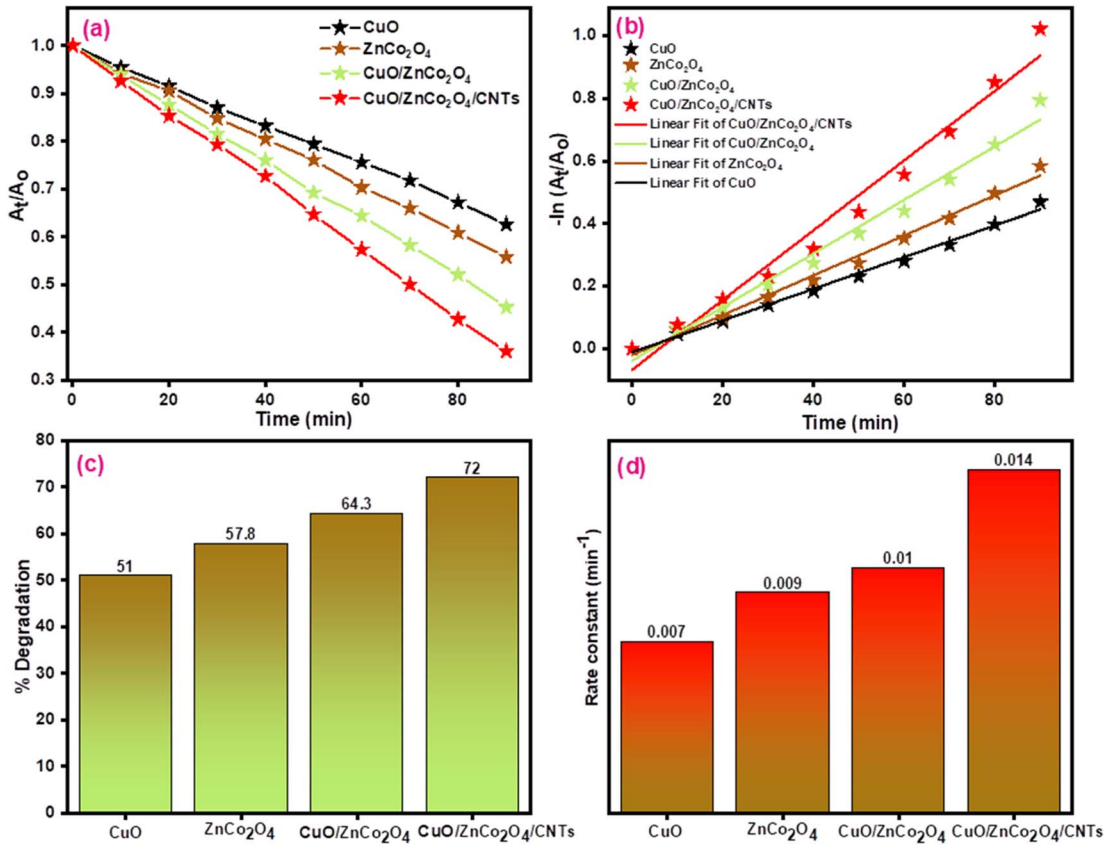

Fig. 18 (a and b) Kinetic plots (c) % degradation, and (d) rate constant plot for phenol degradation using CuO, $ZnCo_2O_4$, $CuO/ZnCo_2O_4$, and $CuO/ZnCo_2O_4$/CNTs.

Table 6 Calculated parameters for phenol degradation using various photocatalysts

Photocatalyst	Degradation (%)	k (min^{-1})	$t_{1/2}$ (min)	R^2
CuO	51	0.007	99.0	0.995
$ZnCo_2O_4$	57.8	0.009	77	0.979
$CuO/ZnCo_2O_4$	64.3	0.010	69.31	0.974
$CuO/ZnCo_2O_4$/CNTs	72	0.014	49.5	0.977

the CV decolorization. Four photocatalytic cycles were used to test the reusability of the material. Fig. 19(a) shows the recyclability plot of $CuO/ZnCo_2O_4$/CNTs photocatalyst for the removal of CV dye. After each cycle, there was a very small decrease in the % photodegradation using $CuO/ZnCo_2O_4$/CNTs (Fig. 19b). After the first cycle, the photocatalyst degrades 87.7% of CV dye. The result demonstrated that even after four cycles, the $CuO/ZnCo_2O_4$/CNTs retained 80% degrading efficiency. Actually, the total catalyst efficiency was reduced by the adsorption of organic intermediates and during the process of washing after every cycle run.[82]

4.5. Trapping tests

A scavenging mechanism was employed to examine the roles of various photo-active species in the photocatalytic degradation of CV dye using $CuO/ZnCo_2O_4$/CNTs, with different quenchers present. Salicylic acid and 2-propanol were used to quench hydroxyl radicals.[83] While ethylenediaminetetraacetic acid (EDTA) and silver nitrate ($AgNO_3$) were used to quench holes and electrons respectively. The trapping experiment was examined using the same photocatalytic process (Fig. 20).

The results demonstrate that $OH^{\bullet}$ is the main active species in the degradation of crystal violet because it represents the minimum degradation as compared to other scavengers. $CuO/ZnCo_2O_4$/CNTs degrade, 55.1% of CV dye in the presence of 2-propanol and 51.7% in the presence of salicylic acid. CV dye shows degradation of 76.5% in the presence of EDTA and 84.2% in the presence of silver nitrate. Table 7 shows the parameters calculated for CV degradation in the presence of scavengers. The activity displayed by photo-reactive species in the degradation of CV dye follows the following order.

$$OH^{\bullet} > h^{+} > e^{-} \quad (8)$$

5. Photodegradation mechanism

The pollutant degradation pathway using $CuO/ZnCo_2O_4$/CNTs is shown in Fig. 21. Eqn (9) and (10) were used to determine the values of the valence band potential (E_{VB}) and conduction band potential (E_{CB}).

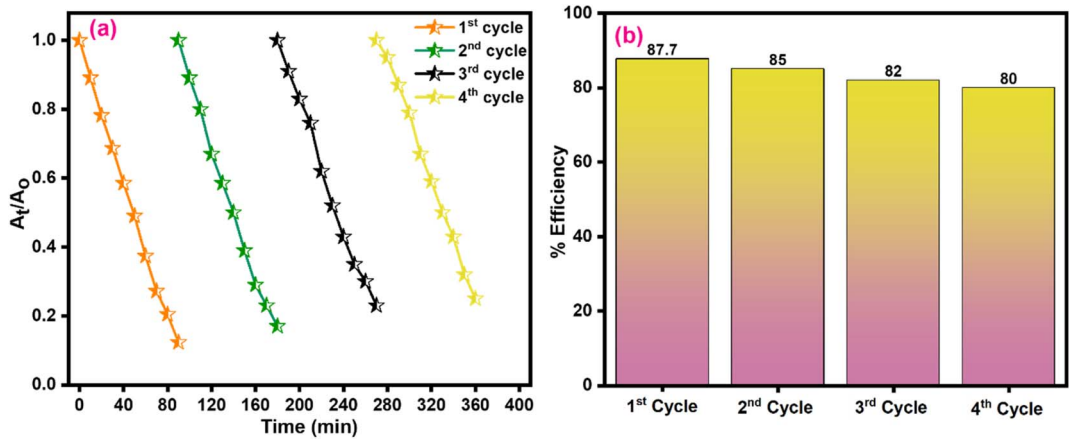

Fig. 19 (a) A_t/A_o *vs.* time plot of CV dye degradation by CuO/$ZnCo_2O_4$/CNTs and (b) % efficiency shown by the CuO/$ZnCo_2O_4$/CNTs for the removal of CV dye for four consecutive cycles.

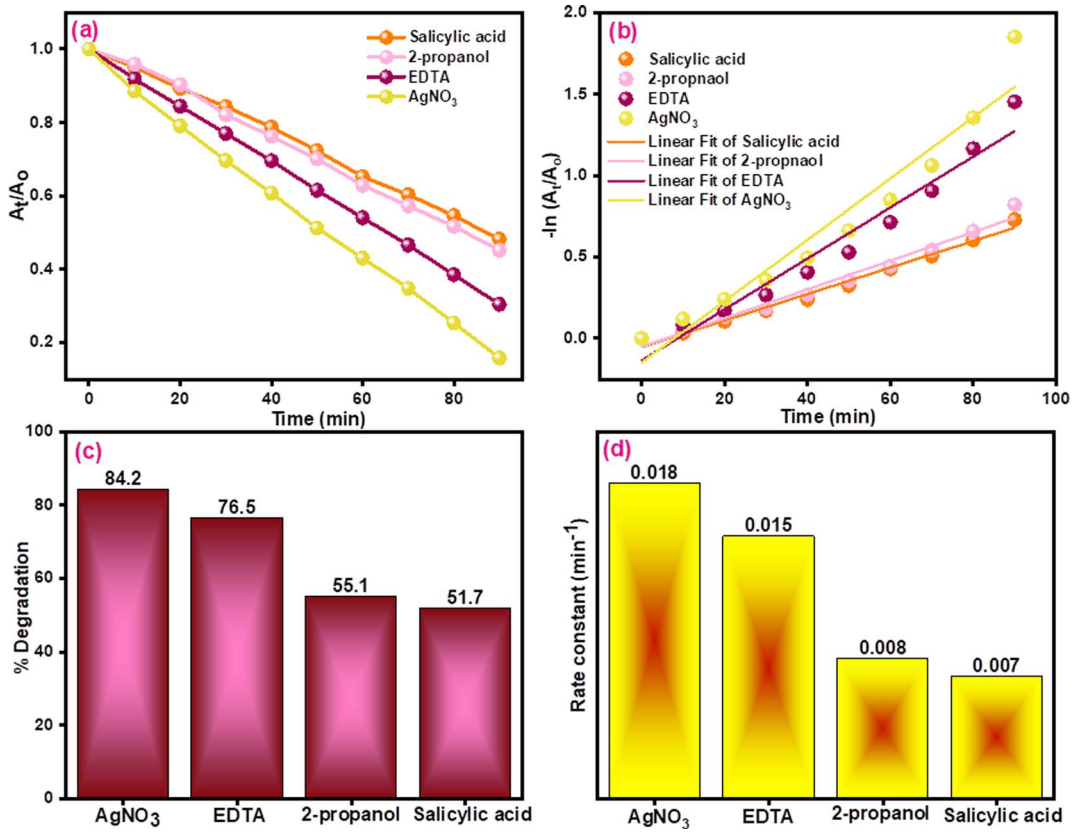

Fig. 20 Scavenging plots for CV dye degradation (a) A_t/A_o *vs.* time (b) $-\ln A_t/A_o$ *vs.* time (c) % degradation, and (d) rate constant plot in the presence of different quenchers using CuO/$ZnCo_2O_4$/CNTs.

$$E_{CB} = \chi - E^e - 0.5E_g \quad (9)$$

$$E_{VB} = E_g + E_{CB} \quad (10)$$

In this case, χ denotes absolute electronegativity, E^e is the energy of free electrons, E_g is the band gap energy.

When the CuO/$ZnCo_2O_4$/CNTs photocatalyst is exposed to visible light, the excited electrons move from the valence band

Table 7 Calculated parameters for CV degradation in the presence of scavengers

Photocatalyst	% degradation	k (min^{-1})	$t_{1/2}$ (min)	R^2
Salicylic acid	51.7	0.007	99.01	0.984
2-Propanol	55.1	0.008	86.63	0.979
EDTA	76.5	0.015	46.20	0.956
$AgNO_3$	84.2	0.018	38.50	0.941

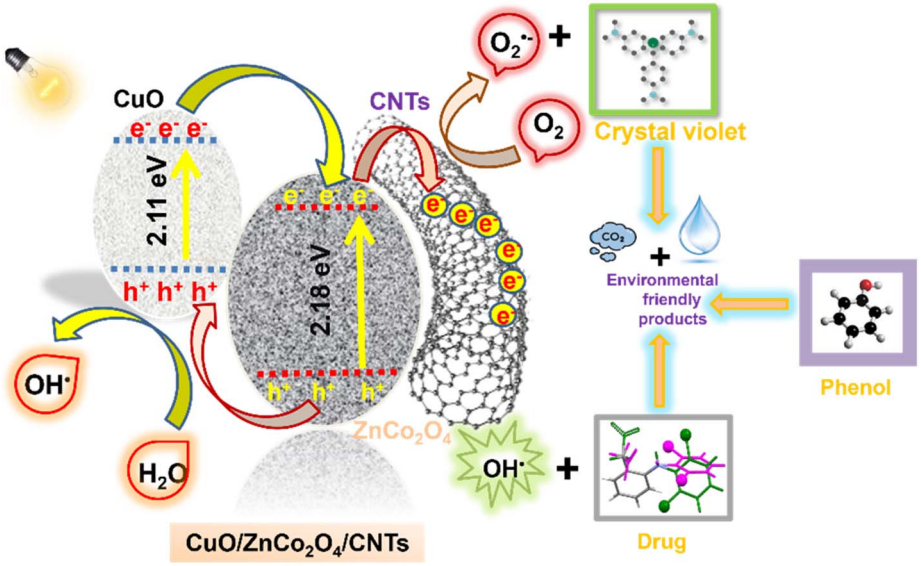

Fig. 21 Mechanism of degradation of pollutants by $CuO/ZnCo_2O_4/CNTs$.

to the conduction band, leaving holes behind. Subsequently, the photoexcited electrons transfer from the conduction band (CB) of CuO to the CB of $ZnCo_2O_4$. This causes the abundance of electrons in $ZnCo_2O_4$. These electrons are then trapped by CNTs. Meanwhile, VB of CuO became hole-rich. These photogenerated electrons react with O_2 to form $O_2^{\cdot-}$, which then contributes to the degradation of pollutants through a series of reactions. On the surface of the $CuO/ZnCo_2O_4/CNTs$, holes and

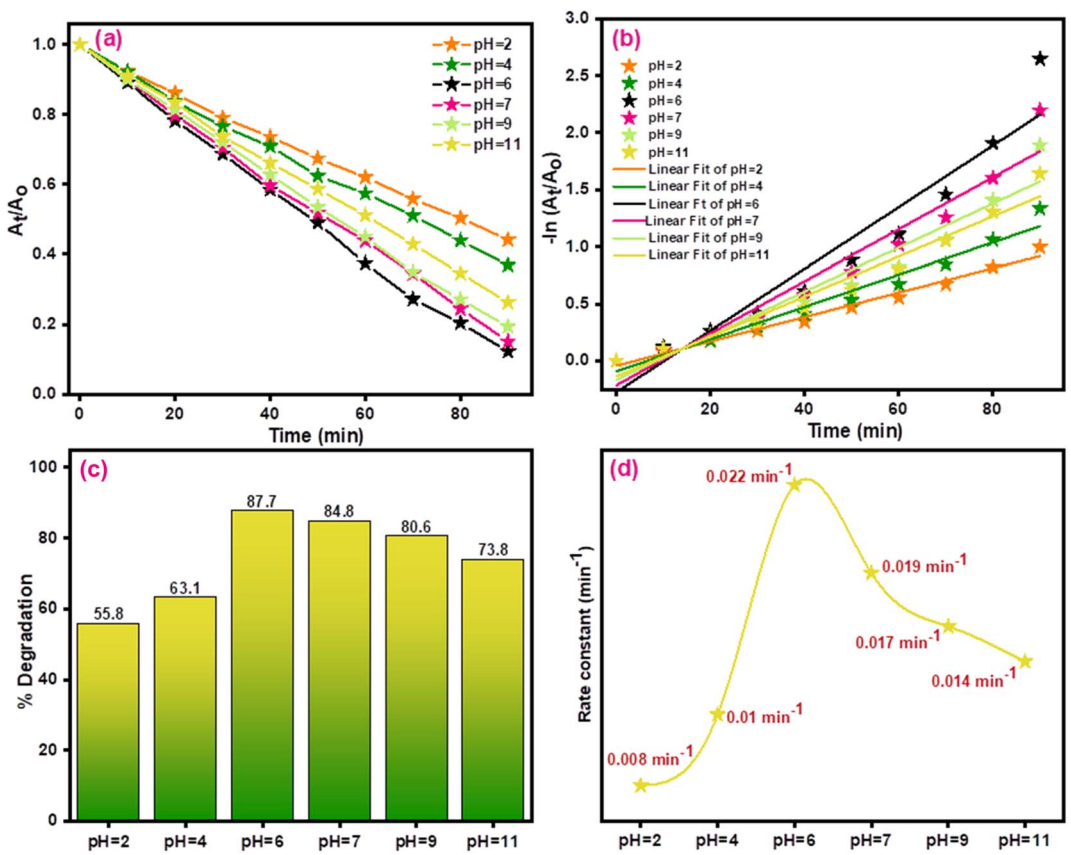

Fig. 22 Effect of pH on CV dye degradation (a and b) kinetics plots, (c) % degradation and (d) rate constant under $CuO/ZnCo_2O_4/CNTs$.

electrons cause oxidation–reduction reactions. These reactions produced hydroxyl radicals. When these $O_2^{\bullet -}$ and $OH^{\bullet}$ degrade the pollutants, environmentally safe byproducts (CO_2 and H_2O) are produced. The following equations illustrate the photocatalytic mechanism.

$$CuO/ZnCo_2O_4 + h\nu \rightarrow CuO(e_{C.B}^- + h_{V.B}^+) + ZnCo_2O_4(e_{C.B}^- + h_{V.B}^+) \quad (11)$$

$$ZnCo_2O_4(e_{C.B}^-) + CNTs \rightarrow CNTs(e^-) + ZnCo_2O_4 \quad (12)$$

$$CNTs(e^-) + O_2 \rightarrow O_2^{\bullet -} + CNTs \quad (13)$$

$$CuO(h_{V.B}^+) + H_2O \rightarrow H^+ + OH^- + CuO \quad (14)$$

$$CuO(h_{V.B}^+) + OH^- \rightarrow CuO + OH^{\bullet} \quad (15)$$

$$O_2^{\bullet -} + OH^{\bullet} + \text{pollutants} \rightarrow \text{degradation products} \quad (16)$$

6. Effect of pH

The photo-oxidation of organic dyes is significantly impacted by the wide range of pH levels of the wastewater from different industries. Solutions with varying pH values (2, 4, 6, 7, 9, and 11) were used to examine the impact of the initial pH of the CV dye. The pH was maintained by using solutions of sodium hydroxide (0.2 M) and hydrochloric acid (0.2 M). Fig. 22(a–d) shows the behavior of CV dye solutions of various pH in the presence of $CuO/ZnCo_2O_4$/CNTs. The results showed that the CV dye degradation rate was higher at pH values between 6 and 11 as compared pH 2 and 4. This trend suggests that the rate of dye degradation onto the surface of the $CuO/ZnCo_2O_4$/CNTs is maximum at pH = 6. CV dye was found to degrade at a maximal rate of $k = 0.022\ min^{-1}$, which drops sharply to $0.019\ min^{-1}$ at pH 7. The electrostatic connection between the substrate and photocatalyst surfaces was linked to the degradation patterns at basic and acidic pH levels.[84] The percentage of dye degradation was low at acidic pH. This could be because of the increased development of H^+ ions on the surface of the photocatalyst, which reduced the rate of degradation and the adsorption of molecules. Higher pH values resulted in increased degradation efficiency because more hydroxyl radicals were generated owing to the greater concentration of OH^- ions in the alkaline medium.

7. Effect of dye concentration

In order to further investigate the efficiency of the prepared $CuO/ZnCo_2O_4$/CNTs, the effect of dye concentration was examined. The degree of photocatalytic reaction rate at the surface of the photocatalyst can be influenced by the initial dye concentration. When the concentration of dye is high, there will be

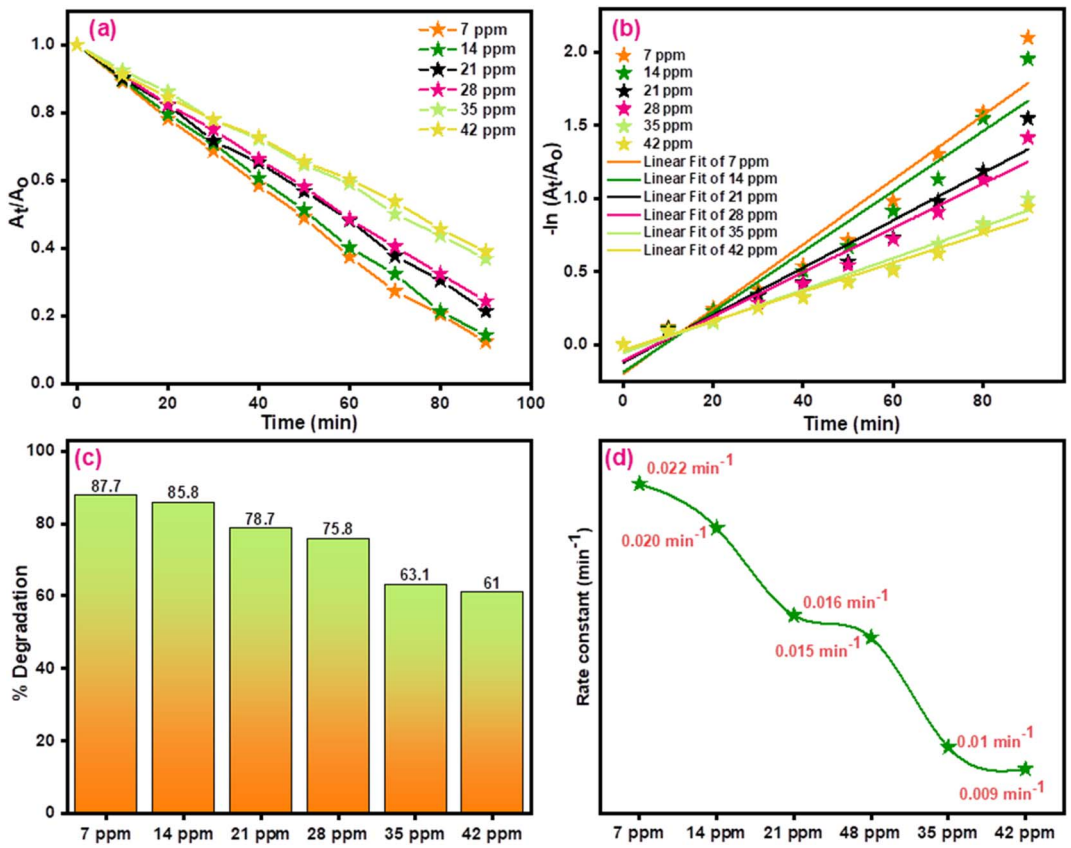

Fig. 23 Effect of dye concentration on (a and b) kinetics plots of CV dye, (c) % degradation and (d) rate constant under $CuO/ZnCo_2O_4$/CNTs.

intense competition among the dye molecules to become adsorbed on the photocatalyst surface.[85] The process of photodegradation finally slows down or stops. Therefore, the experiments were conducted under $CuO/ZnCo_2O_4$/CNTs with varying dye (CV) concentrations to investigate the concentration effect. The findings are shown in Fig. 23(a–d).

The rate and degradation of the dye decreased as the concentration of CV increased. For 7 ppm, the degradation percentage was 87.7% and for 42 ppm, the degradation dropped to 61%. The obtained results showed that increasing dye concentration provides a larger number of dye molecules, which in turn enhances competition for the adsorption process. The active sites are coated with dye molecules, which lower the percentage of degradation.

8. Effect of catalyst dosage

The photocatalyst dosage affects the surface area, light absorption efficiency, and photo-removal process for organic dyes.[82,86] Photocatalytic tests were conducted with varying concentrations of $CuO/ZnCo_2O_4$/CNTs (5–40 mg) in order to examine the dosage effect on CV dye degradation. The outcomes are shown in Fig. 24(a–d).

It is evident from the results that an increase in catalyst concentration is correlated with a rise in the photodegradation percentage. When the dosage of photocatalyst was increased from 5 mg to 30 mg, the rate of CV dye degradation increased as well. The percentage degradation of CV dye did not significantly change with an additional increase in catalyst dosage. At a catalytic dosage of 30 mg, the highest degradation rate of 87.7% was noted. Actually, more light exposure increases the capacity of the $CuO/ZnCo_2O_4$/CNTs to absorb photons and ultimately enhances photocatalytic efficiency. The availability of a higher surface area for the adsorption of additional dye molecules and the rise in the mass to volume ratio of photocatalyst are both credited with the increase in the rate of CV dye degradation.

9. Conclusions

In this work, CNTs were introduced into $CuO/ZnCo_2O_4$ using a sonication technique to synthesize $CuO/ZnCo_2O_4$/CNTs nanocomposite. Various physicochemical aspects of the prepared photocatalysts, such as phase identification, morphology, purity, and optical properties, were identified through XRD, FESEM, EDS, and UV-Vis spectroscopy. The band gap values of the prepared photocatalysts followed the order $ZnCo_2O_4$ > CuO > $CuO/ZnCo_2O_4$ > $CuO/ZnCo_2O_4$/CNTs. The rate constant value for the degradation of CV dye, diclofenac sodium, and phenol using $CuO/ZnCo_2O_4$/CNTs was found to be 0.022, 0.016, and 0.014 min^{-1} respectively. After being exposed to visible light, $CuO/ZnCo_2O_4$/CNTs showed high percentage

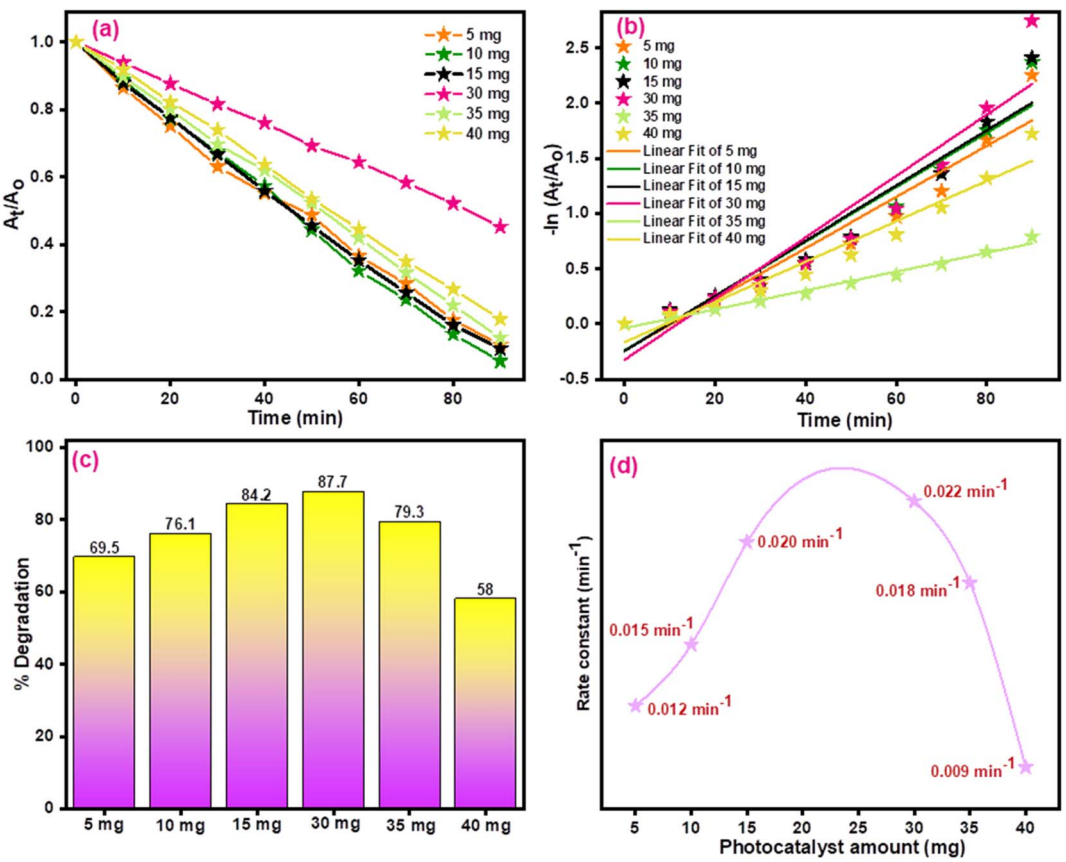

Fig. 24 Effect of catalyst dosage on (a and b) kinetics plots of CV dye, (c) % degradation and (d) rate constant under $CuO/ZnCo_2O_4$/CNTs.

degradation of 87.7% of the CV dye, whereas the % degradation of diclofenac sodium and phenol were found to be 82% and 72% respectively. Among all the photocatalysts, the highest degradation efficiency was achieved with $CuO/ZnCo_2O_4$/CNTs for all pollutants examined in this study, owing to the presence of CNTs in the composite that offers enhanced surface area and active sites for the rapid and efficient breakdown of organic contaminants.

Data availability

All data generated or analyzed during this study are included in this article.

Conflicts of interest

The authors declare that there is no conflict of interest.

Acknowledgements

The authors express their gratitude to Princess Nourah bint Abdulrahman University Researchers Supporting Project number (PNURSP2024R450), Princess Nourah bint Abdulrahman University, Riyadh, Saudi Arabia. Prof. Dr Sonia Zulfiqar extends her heartfelt thanks to the Statutory City of Ostrava, Czechia, for their support through the Research Grant "Global Experts". Prof. Cochran and Zulfiqar express their gratitude to the National Science Foundation for financial support through research grants NSF-2113695, NSF-2218070 and NSF-2242763. The authors are also thankful to the Deanship of Scientific Research, Islamic University of Madinah, Madinah (Saudi Arabia) for support *via* post publishing program.

References

1 P. Rajasulochana and V. Preethy, Comparison on efficiency of various techniques in treatment of waste and sewage water–A comprehensive review, *Resour.-Effic. Technol.*, 2016, **2**, 175–184.

2 M. F. Abou Taleb, M. Afaq, H. A. Albalwi, F. I. Abou El Fadl, A. Irshad and M. M. Ibrahim, Tb-doped $BiFeO_3$ nanostructure and its composite with CNTs to improve the light-harvesting properties, *Mater. Sci. Eng., B*, 2024, **299**, 116916.

3 L. Schweitzer and J. Noblet, Water contamination and pollution, *Green Chem.*, 2018, 261–290.

4 K. M. Katubi, S. Akbar, A. Habib, Z. Alrowaili, M. Al-Buriahi, A. Irshad and M. F. Warsi, Fabrication of CNTs supported $CuCo_2O_4/Co_3S_4$ composite for advanced photocatalytic application, *Optik*, 2024, **300**, 171653.

5 S. Sohrabnezhad, A. Pourahmad and E. Radaee, Photocatalytic degradation of basic blue 9 by CoS nanoparticles supported on AlMCM-41 material as a catalyst, *J. Hazard. Mater.*, 2009, **170**, 184–190.

6 A. Singh, S. S. Shah, C. Sharma, V. Gupta, A. K. Sundramoorthy, P. Kumar and S. Arya, An approach towards different techniques for detection of heavy metal ions and their removal from wastewater, *J. Environ. Chem. Eng.*, 2024, 113032.

7 A. Ahmed, A. Singh, B. Padha, A. K. Sundramoorthy, A. Tomar and S. Arya, UV–vis spectroscopic method for detection and removal of heavy msetal ions in water using Ag doped ZnO nanoparticles, *Chemosphere*, 2022, **303**, 135208.

8 J. Arshad, F. M. A. Alzahrani, M. F. Warsi, U. Younis, M. Anwar, Z. Alrowaili, M. Al-Buriahi and A. Manzoor, Copper substituted spinel Co–Cr spinel Ferrites@ Graphitic carbon nitride nanocomposite as a visible light active photocatalytic material, *Opt. Mater.*, 2024, **148**, 114906.

9 N. Alfryyan, M. Ikram, A. Manzoor, A. Jamil, Z. Alrowaili, M. Al-Buriahi, A. Irshad and M. I. Din, Synthesis of Cd-substituted $NiCoPrFe_2O_4$@ CNTs via sol-gel method: Investigating the structural and photocatalytic properties, *Phys. B*, 2023, **660**, 414885.

10 D. Lu, Y. Zhang, S. Lin, L. Wang and C. Wang, Synthesis of magnetic $ZnFe_2O_4$/graphene composite and its application in photocatalytic degradation of dyes, *J. Alloys Compd.*, 2013, **579**, 336–342.

11 R. V. Prihod'ko and N. M. Soboleva, Photocatalysis: Oxidative processes in water treatment, *J. Chem.*, 2013, **2013**, 168701.

12 K. Kannan, D. Radhika, D. Gnanasangeetha, S. K. Lakkaboyana, K. K. Sadasivuni, K. Gurushankar and M. M. Hanafiah, Photocatalytic and antimicrobial properties of microwave synthesized mixed metal oxide nanocomposite, *Inorg. Chem. Commun.*, 2021, **125**, 108429.

13 A. Singh, A. Ahmed, A. Sharma, C. Sharma, S. Paul, A. Khosla, V. Gupta and S. Arya, Promising photocatalytic degradation of methyl orange dye via sol-gel synthesized Ag–CdS@ Pr-TiO_2 core/shell nanoparticles, *Phys. B*, 2021, **616**, 413121.

14 D. Ravelli, D. Dondi, M. Fagnoni and A. Albini, Photocatalysis. A multi-faceted concept for green chemistry, *Chem. Soc. Rev.*, 2009, **38**, 1999–2011.

15 M. Kumar, B. Abebe, H. Nagaswarupa, H. Murthy, C. Ravikumar and F. Sabir, Enhanced photocatalytic and electrochemical performance of TiO_2–Fe_2O_3 nanocomposite: its applications in dye decolorization and as supercapacitors, *Sci. Rep.*, 2020, **10**, 1249.

16 A. Shabbir, S. Ajmal, M. Shahid, I. Shakir, P. O. Agboola and M. F. Warsi, Zirconium substituted spinel nano-ferrite $Mg_{0.2}Co_{0.8}Fe_2O_4$ particles and their hybrids with reduced graphene oxide for photocatalytic and other potential applications, *Ceram. Int.*, 2019, **45**, 16121–16129.

17 K. Nakata and A. Fujishima, TiO_2 photocatalysis: Design and applications, *J. Photochem. Photobiol., C*, 2012, **13**, 169–189.

18 M. F. Warsi, B. Bashir, S. Zulfiqar, M. Aadil, M. U. Khalid, P. O. Agboola, I. Shakir, M. A. Yousuf and M. Shahid, $Mn_{1-x}Cu_xO_2$/reduced graphene oxide nanocomposites: synthesis, characterization, and evaluation of visible light mediated catalytic studies, *Ceram. Int.*, 2021, **47**, 5044–5053.

19 A. K. Sibhatu, G. K. Weldegebrieal, S. Sagadevan, N. N. Tran and V. Hessel, Photocatalytic activity of CuO nanoparticles

for organic and inorganic pollutants removal in wastewater remediation, *Chemosphere*, 2022, **300**, 134623.

20 Y. Al-Douri, S. Abdulateef, A. A. Odeh, C. Voon and N. Badi, GaNO colloidal nanoparticles synthesis by nanosecond pulsed laser ablation: Laser fluence dependent optical absorption and structural properties, *Powder Technol.*, 2017, **320**, 457–461.

21 J.-P. Jolivet, M. Henry and J. Livage, *Metal Oxide Chemistry and Synthesis: From Solution to Solid State*, 2000.

22 A.-Z. Warsi, O. K. Hussien, A. Iftikhar, F. Aziz, D. Alhashmialameer, S. F. Mahmoud, M. F. Warsi and D. I. Saleh, Co-precipitation assisted preparation of Ag_2O, CuO and Ag_2O/CuO nanocomposite: characterization and improved solar irradiated degradation of colored and colourless organic effluents, *Ceram. Int.*, 2022, **48**, 19056–19067.

23 A. Tadjarodi, O. Akhavan and K. Bijanzad, Photocatalytic activity of CuO nanoparticles incorporated in mesoporous structure prepared from bis (2-aminonicotinato) copper (II) microflakes, *Trans. Nonferrous Met. Soc. China*, 2015, **25**, 3634–3642.

24 S. Harish, J. Archana, M. Sabarinathan, M. Navaneethan, K. Nisha, S. Ponnusamy, C. Muthamizhchelvan, H. Ikeda, D. Aswal and Y. Hayakawa, Controlled structural and compositional characteristic of visible light active ZnO/CuO photocatalyst for the degradation of organic pollutant, *Appl. Surf. Sci.*, 2017, **418**, 103–112.

25 R. Katal, S. Masudy-panah, E. Y.-J. Kong, N. D. Khiavi, M. H. D. A. Farahani and X. Gong, Nanocrystal-engineered thin CuO film photocatalyst for visible-light-driven photocatalytic degradation of organic pollutant in aqueous solution, *Catal. Today*, 2020, **340**, 236–244.

26 S. S. Hossain, M. Tarek, T. D. Munusamy, K. M. R. Karim, S. M. Roopan, S. M. Sarkar, C. K. Cheng and M. M. R. Khan, Facile synthesis of CuO/CdS heterostructure photocatalyst for the effective degradation of dye under visible light, *Environ. Res.*, 2020, **188**, 109803.

27 A. ur Rehman, M. Aadil, S. Zulfiqar, P. O. Agboola, I. Shakir, M. F. A. Aboud, S. Haider and M. F. Warsi, Fabrication of binary metal doped CuO nanocatalyst and their application for the industrial effluents treatment, *Ceram. Int.*, 2021, **47**, 5929–5937.

28 H. Benhebal, C. Wolfs, S. Kadi, R. G. Tilkin, B. Allouche, R. Belabid, V. Collard, A. Felten, P. Louette and S. D. Lambert, Visible light sensitive SnO_2/$ZnCo_2O_4$ material for the photocatalytic removal of organic pollutants in water, *Inorganics*, 2019, **7**, 77.

29 K. Gurunathan, J.-O. Baeg, S. M. Lee, E. Subramanian, S.-J. Moon and K.-j. Kong, Visible light active pristine and Fe^{3+} doped $CuGa_2O_4$ spinel photocatalysts for solar hydrogen production, *Int. J. Hydrogen Energy*, 2008, **33**, 2646–2652.

30 Y. Yao, F. Lu, Y. Zhu, F. Wei, X. Liu, C. Lian and S. Wang, Magnetic core–shell $CuFe_2O_4$@ C_3N_4 hybrids for visible light photocatalysis of Orange II, *J. Hazard. Mater.*, 2015, **297**, 224–233.

31 S. Sharma, V. Dutta, P. Raizada, A. Hosseini-Bandegharaei, V. Thakur, V.-H. Nguyen, Q. VanLe and P. Singh, An overview of heterojunctioned $ZnFe_2O_4$ photocatalyst for enhanced oxidative water purification, *J. Environ. Chem. Eng.*, 2021, **9**, 105812.

32 B. Basha, M. Ikram, Z. Alrowaili, M. Al-Buriahi, M. Anwar and M. Suleman, Wet chemical route synthesis of Cr doped $CoFe_2O_4$@ rGO nanocomposite for photodegradation of organic effluents present in drinking water, *Ceram. Int.*, 2023, **49**, 30049–30059.

33 I. A. Mkhalid, A. A. Ismail, M. A. Hussein and R. H. Al Thomali, Nanoheterojunctions $MnCo_2O_4$ nanoparticles anchored on mesoporous TiO_2 networks for superior photocatalytic ability, *Mater. Res. Bull.*, 2023, **167**, 112439.

34 L. Liu, L. Zuo, R. Li, T. Xi, H. Fan, B. Li and L. Wang, Novel $CoMn_2O_4$-$ZnIn_2S_4$ hollow heterostructure cage for efficient photocatalytic hydrogen evolution, *Appl. Surf. Sci.*, 2023, **635**, 157646.

35 H. Guo, J. Chen, W. Weng, Q. Wang and S. Li, Facile template-free one-pot fabrication of $ZnCo_2O_4$ microspheres with enhanced photocatalytic activities under visible-light illumination, *Chem. Eng. J.*, 2014, **239**, 192–199.

36 G.-Y. Zhang, B. Guo and J. Chen, MCo_2O_4 (M= Ni, Cu, Zn) nanotubes: template synthesis and application in gas sensors, *Sens. Actuators, B*, 2006, **114**, 402–409.

37 Y. Sharma, N. Sharma, G. Subba Rao and B. Chowdari, Nanophase $ZnCo_2O_4$ as a high performance anode material for Li-ion batteries, *Adv. Funct. Mater.*, 2007, **17**, 2855–2861.

38 H. Jung, T.-T. Pham and E. W. Shin, Effect of g-C_3N_4 precursors on the morphological structures of g-C_3N_4/ZnO composite photocatalysts, *J. Alloys Compd.*, 2019, **788**, 1084–1092.

39 B. Cui, H. Lin, X.-C. Zhao, J.-B. Li and W.-D. Li, Visible light induced photocatalytic activity of $ZnCo_2O_4$ nanoparticles, *Acta Phys.-Chim. Sin.*, 2011, **27**, 2411–2415.

40 T. Chang, Z. Li, G. Yun, Y. Jia and H. Yang, Enhanced photocatalytic activity of ZnO/CuO nanocomposites synthesized by hydrothermal method, *Nanomicro Lett.*, 2013, **5**, 163–168.

41 M. Taufique, A. Haque, P. Karnati and K. Ghosh, ZnO–CuO nanocomposites with improved photocatalytic activity for environmental and energy applications, *J. Electron. Mater.*, 2018, **47**, 6731–6745.

42 K. Goswami, R. Ananthakrishnan and S. Mandal, Facile synthesis of cation doped ZnO-$ZnCo_2O_4$ hetero-nanocomposites for photocatalytic decomposition of aqueous organics under visible light, *Mater. Chem. Phys.*, 2018, **206**, 174–185.

43 B. Tan, Y. Fang, Q. Chen, X. Ao and Y. Cao, Preparation of a $CaFe_2O_4$/$ZnCo_2O_4$ composite material and its photocatalytic degradation of tetracycline, *Opt. Mater.*, 2020, **109**, 110470.

44 D. Upadhaya and D. D. Purkayastha, Self-cleaning activity of CuO/ZnO heterostructure: A synergy of photocatalysis and hydrophilicity, *J. Taiwan Inst. Chem. Eng.*, 2022, **132**, 104216.

45 L. Zhu, H. Li, Z. Liu, P. Xia, Y. Xie and D. Xiong, Synthesis of the 0D/3D CuO/ZnO heterojunction with enhanced photocatalytic activity, *J. Phys. Chem. C*, 2018, **122**, 9531–9539.

46 R. Jahanshahi, A. Mohammadi, M. Doosti, S. Sobhani and J. M. Sansano, $ZnCo_2O_4$/g-C_3N_4/Cu nanocomposite as a new efficient and recyclable heterogeneous photocatalyst with enhanced photocatalytic activity towards the metronidazole degradation under the solar light irradiation, *Environ. Sci. Pollut. Res.*, 2022, **29**, 65043–65060.

47 Z. Li, B. Gao, G. Z. Chen, R. Mokaya, S. Sotiropoulos and G. L. Puma, Carbon nanotube/titanium dioxide (CNT/TiO_2) core–shell nanocomposites with tailored shell thickness, CNT content and photocatalytic/photoelectrocatalytic properties, *Appl. Catal., B*, 2011, **110**, 50–57.

48 S. Song, B. Cheng, N. Wu, A. Meng, S. Cao and J. Yu, Structure effect of graphene on the photocatalytic performance of plasmonic Ag/Ag_2CO_3-rGO for photocatalytic elimination of pollutants, *Appl. Catal., B*, 2016, **181**, 71–78.

49 X. An and C. Y. Jimmy, Graphene-based photocatalytic composites, *RSC Adv.*, 2011, **1**, 1426–1434.

50 Y. Pan, X. Liu, W. Zhang, Z. Liu, G. Zeng, B. Shao, Q. Liang, Q. He, X. Yuan and D. Huang, Advances in photocatalysis based on fullerene C60 and its derivatives: Properties, mechanism, synthesis, and applications, *Appl. Catal., B*, 2020, **265**, 118579.

51 M. Aadil, S. Zulfiqar, M. Shahid, P. O. Agboola, S. Haider, M. F. Warsi and I. Shakir, Fabrication of rationally designed CNTs supported binary nanohybrid with multiple approaches to boost electrochemical performance, *J. Electroanal. Chem.*, 2021, **884**, 115070.

52 M. Ahmad, I. Ahmad, E. Ahmed, M. S. Akhtar and N. Khalid, Facile and inexpensive synthesis of Ag doped ZnO/CNTs composite: Study on the efficient photocatalytic activity and photocatalytic mechanism, *J. Mol. Liq.*, 2020, **311**, 113326.

53 D. Saravanakkumar, H. Abou Oualid, Y. Brahmi, A. Ayeshamariam, M. Karunanaithy, A. M. Saleem, K. Kaviyarasu, S. Sivaranjani and M. Jayachandran, Synthesis and characterization of CuO/ZnO/CNTs thin films on copper substrate and its photocatalytic applications, *OpenNano*, 2019, **4**, 100025.

54 M. Priya, S. Udhayan, P. Vasantharani and G. Sivakumar, Energy storage performance and photocatalytic activity of Diamond-like ZnCo2O4 nanostructure, Inor, *Chem. Commun.*, 2023, **153**, 110762.

55 C. Wang, H. Wang, L. Li, R. Zhao, J. Han and L. Wang, Hollow rod-shaped Cu-In-Zn-S@ $ZnCo_2O_4$@ In_2O_3 tandem heterojunction for efficient visible light-induced photocatalytic hydrogen production, *Fuel*, 2024, **355**, 129537.

56 M. Ahmad, E. Ahmed, Z. Hong, X. Jiao, T. Abbas and N. Khalid, Enhancement in visible light-responsive photocatalytic activity by embedding Cu-doped ZnO nanoparticles on multi-walled carbon nanotubes, *Appl. Surf. Sci.*, 2013, **285**, 702–712.

57 A. Muthuvel, M. Jothibas and C. Manoharan, Synthesis of copper oxide nanoparticles by chemical and biogenic methods: photocatalytic degradation and in vitro antioxidant activity, *Nanotechnol. Environ. Eng.*, 2020, **5**, 14.

58 X. Song, Q. Ru, B. Zhang, S. Hu and B. An, Flake-by-flake $ZnCo_2O_4$ as a high capacity anode material for lithium-ion battery, *J. Alloys Compd.*, 2014, **585**, 518–522.

59 M. Ikram, M. M. Baig, I. Shakir, A. Irshad, Z. A. ALOthman, M. F. Warsi and S. G. Lee, Boosting the electrochemical properties of MoO_3/$MnFe_2O_4$/MXene for high-performance supercapacitor applications, *J. Energy Storage*, 2024, **90**, 111746.

60 S. H. Kim, A. Umar and S.-W. Hwang, Rose-like CuO nanostructures for highly sensitive glucose chemical sensor application, *Ceram. Int.*, 2015, **41**, 9468–9475.

61 S. S. Abdullaev, Y. F. Breesam, A. A. AlZubaidi, A. K. Tripathi, A. Kareem, S. V. Kuznetsov, T. Alawsi and R. S. Zabibah, ZnO@ $ZnCo_2O_4$ core-shell: a novel high electrocatalytic nanostructure to replace platinum as the counter electrode in dye-sensitized solar cells, *Mater. Sci. Semicond. Process.*, 2023, **165**, 107709.

62 A. Sivakumar, S. Soundarya, S. S. Jude Dhas, K. K. Bharathi and S. M. B. Dhas, Shock wave driven solid state phase transformation of Co_3O_4 to CoO nanoparticles, *J. Phys. Chem. C*, 2020, **124**, 10755–10763.

63 S. Li, Z. Hou, Z. Cheng, H. Lian, C. Li and J. Lin, Enhanced near-infrared quantum cutting luminescence in 1, 2, 4, 5-benzenetetracarboxylic acid/NaYF4: Tb^{3+}, Yb^{3+} hybrid nanoparticles, *RSC Adv.*, 2013, **3**, 5491–5497.

64 M. U. Khalid, K. M. Katubi, S. Zulfiqar, Z. Alrowaili, M. Aadil, M. Al-Buriahi, M. Shahid and M. F. Warsi, Boosting the electrochemical activities of MnO_2 for next-generation supercapacitor application: adaptation of multiple approaches, *Fuel*, 2023, **343**, 127946.

65 M. Aadil, A. G. Taki, S. Zulfiqar, A. Rahman, M. Shahid, M. F. Warsi, Z. Ahmad, A. A. Alothman and S. Mohammad, Gadolinium doped zinc ferrite nanoarchitecture reinforced with a carbonaceous matrix: a novel hybrid material for next-generation flexible capacitors, *RSC Adv.*, 2023, **13**, 28063–28075.

66 D. Arun Kumar, J. Merline Shyla and F. P. Xavier, Synthesis and characterization of TiO_2/SiO_2 nano composites for solar cell applications, *Appl. Nanosci.*, 2012, **2**, 429–436.

67 A. K. Thakur, A. B. Deshmukh, R. B. Choudhary, I. Karbhal, M. Majumder and M. V. Shelke, Facile synthesis and electrochemical evaluation of PANI/CNT/MoS_2 ternary composite as an electrode material for high performance supercapacitor, *Mater. Sci. Eng. B*, 2017, **223**, 24–34.

68 M. Y. Guo, F. Liu, Y. H. Leung, A. M. C. Ng, A. B. Djurišić and W. K. Chan, TiO_2–carbon nanotube composites for visible photocatalysts–Influence of TiO_2 crystal structure, *Curr. Appl. Phys.*, 2013, **13**, 1280–1287.

69 M. Ikram, A. Irshad, K. M. Katubi, Z. Alrowaili, M. Al-Buriahi and M. F. Warsi, Enhanced electrochemical activity of chemically engineered rGO-decorated NiO/$CoFe_2O_4$ for supercapacitor applications, *Ceram. Int.*, 2024, **50**, 19578–19591.

70 B. Singh, A. Singh, A. Sharma, P. Mahajan, S. Verma, B. Padha, A. Ahmed and S. Arya, Electrochemical sensing and photocatalytic degradation of 2, 4-dinitrophenol via bismuth (III) oxide nanowires, *J. Mol. Struct.*, 2022, **1255**, 132379.

71 H. Chen, J. Wang, X. Han, F. Liao, Y. Zhang, L. Gao and C. Xu, Facile synthesis of mesoporous $ZnCo_2O_4$ hierarchical microspheres and their excellent supercapacitor performance, *Ceram. Int.*, 2019, **45**, 8577–8584.

72 L. Xie, Y. Liu, H. Bai, C. Li, B. Mao, L. Sun and W. Shi, Core-shell structured $ZnCo_2O_4$@ $ZnWO_4$ nanowire arrays on nickel foam for advanced asymmetric supercapacitors, *J. Colloid Interface Sci.*, 2018, **531**, 64–73.

73 S. Khan, A. Noor, I. Khan, M. Muhammad, M. Sadiq and N. Muhammad, Photocatalytic degradation of organic dyes contaminated aqueous solution using binary $CdTiO_2$ and ternary $NiCdTiO_2$ nanocomposites, *Catalysts*, 2022, **13**, 44.

74 A. Farooq, M. Anwar, H. Somaily, S. Zulfiqar, M. F. Warsi, M. I. Din, A. Muhammad and A. Irshad, Fabrication of Ag-doped magnesium aluminate/rGO composite: a highly efficient photocatalyst for visible light-driven photodegradation of crystal violet and phenol, *Phys. B*, 2023, **650**, 414508.

75 S. M. Botsa and K. Basavaiah, Removal of Nitrophenols from wastewater by monoclinic CuO/RGO nanocomposite, *Nanotechnol. Environ. Eng.*, 2019, **4**, 1–7.

76 H. M. Abo-Dief, S. M. El-Bahy, O. K. Hussein, Z. M. El-Bahy, M. Shahid and I. Shakir, Synthesis and characterization of rGO supported silver doped bimetallic $ZnCo_2O_4$ spinel oxides for enhanced photocatalytic degradation of industrial effluents, *J. Alloys Compd.*, 2022, **913**, 165164.

77 N. Kitchamsetti, D. Narsimulu, A. Chinthakuntla, C. S. Chakra and A. L. de Barros, Bimetallic MOF derived $ZnCo_2O_4$ nanocages as a novel class of high performance photocatalyst for the removal of organic pollutants, *Inorg. Chem. Commun.*, 2022, **144**, 109946.

78 J. Fatima, M. B. Tahir, M. S. Tahir and M. Sagir, Solar driven photocatalytic dye degradation through the novel Ti_2C–$ZnCo_2O_4$MXenes nanocomposite, *Opt. Mater.*, 2022, **133**, 113034.

79 A. Dana and S. Sheibani, CNTs-copper oxide nanocomposite photocatalyst with high visible light degradation efficiency, *Adv. Powder Technol.*, 2021, **32**, 3760–3769.

80 R. S. Shinde, S. D. Khairnar, M. R. Patil, V. A. Adole, P. B. Koli, V. V. Deshmane, D. K. Halwar, R. A. Shinde, T. B. Pawar and B. S. Jagdale, Synthesis and characterization of ZnO/CuO nanocomposites as an effective photocatalyst and gas sensor for environmental remediation, *J. Inorg. Organomet. Polym. Mater.*, 2022, 1–22.

81 F. A. Cataño, G. Cáceres, A. Burgos and R. S. Schrebler, Synthesis and characterization of a ZnO/CuO/Ag composite and its application as a photocatalyst for methyl orange degradation, *Int. J. Electrochem. Sci.*, 2018, **13**, 9242–9256.

82 N. Shaheen, M. F. Warsi, S. Zulfiqar, J. T. Althakafy, A. K. Alanazi, M. I. Din, H. M. Abo-Dief and M. Shahid, La-doped WO_3@ gCN Nanocomposite for Efficient degradation of cationic dyes, *Ceram. Int.*, 2023, **49**, 15507–15526.

83 Y. Chen, C. Chen, Y. Liu and L. Yu, Probing the effect of nitrate anion in CAN: An additional opportunity to reduce the catalyst loading for aerobic oxidations, *Chin. Chem. Lett.*, 2023, **34**, 108489.

84 O. Bechambi, S. Sayadi and W. Najjar, Photocatalytic degradation of bisphenol A in the presence of C-doped ZnO: effect of operational parameters and photodegradation mechanism, *J. Ind. Eng. Chem.*, 2015, **32**, 201–210.

85 S.-M. Lam, J.-C. Sin, A. Z. Abdullah and A. R. Mohamed, Degradation of wastewaters containing organic dyes photocatalysed by zinc oxide: a review, *Desalin. Water Treat.*, 2012, **41**, 131–169.

86 A. Rahman, M. Aadil, M. Akhtar, M. F. Warsi, A. Jamil, I. Shakir and M. Shahid, Magnetically recyclable $Ni_{1-x}Cd_xCe_yFe_{2-y}O_4$-rGO nanocomposite photocatalyst for visible light driven photocatalysis, *Ceram. Int.*, 2020, **46**, 13517–13526.